On Rate-Limiting Mechanisms in Nickel Manganese Cobalt and Lithium Iron Phosphate Cathodes

The Interplay of Low and High Current Constraints

Martin Brischetto

A dissertation
submitted in partial fulfillment of the
requirements for the degree of

Doctor of Philosophy

University of Washington

2026

Reading Committee:
Jihui Yang, Chair
Jie Xiao
Jun Liu

Program Authorized to Offer Degree:
Materials Science & Engineering

University of Washington

Abstract

On Rate-Limiting Mechanisms in Nickel Manganese Cobalt and Lithium Iron Phosphate Cathodes

The Interplay of Low and High Current Constraints

Martin Brischetto

Chair of the Supervisory Committee:

Jihui Yang
Department of Materials Science & Engineering

Lithium-ion batteries lie at the heart of the energy transition away from fossil fuels. They allow us to store intermittent renewable energy and dispatch it on demand in the form of electricity. Mobile applications of lithium-ion batteries, such as in electric vehicles, require high energy densities as the battery needs to propel its own mass, in addition to that of the rest of the car. Much work has been devoted towards this end, with current commercial state-of-the-art lithium-ion batteries reaching energy densities of $200\,\mathrm{Wh\,kg^{-1}}$ to $300\,\mathrm{Wh\,kg^{-1}}$. However, The United States Department of Energy has set the ambitious goal of developing a cell with energy density above $500\,\mathrm{Wh\,kg^{-1}}$ that can cycle for more than 1000 cycles and costs less than $\$60\,\mathrm{kWh^{-1}}$. Increasing the energy density of a cell often involves trade-offs with respect to cycling stability, discharge rate, and cost. Understanding these trade-offs is crucial.

In this dissertation, we develop a physics-based framework for characterizing and understanding discharge curves, rate performance data, and their relationship to the physical rate-limiting mechanisms evolving within the cell. With these models in mind, we assemble the largest, highest resolution, and highest quality rate performance data set of its

kind available in literature; consisting of 58 $LiNi_{0.6}Mn_{0.2}Co_{0.2}O_2$ and 86 $LiFePO_4$ lithium metal anode cells, across five loadings and three porosities, discharged through a densely staggered series of galvanostatic discharge currents.

We identify four different rate-limiting mechanisms that play a role in the capacity underutilization observed in $LiNi_{0.6}Mn_{0.2}Co_{0.2}O_2$ and $LiFePO_4$ cathodes. At low currents, $LiNi_{0.6}Mn_{0.2}Co_{0.2}O_2$ cathodes are limited by the ionic solid-diffusion in the active particles, while $LiFePO_4$ cathodes are limited by the phase-transformation rate of the active particles. We find that the sharp capacity drop at high currents is generally caused by the growing Ohmic and charge-transfer potentials, and not by the ionic liquid-diffusion limits often ascribed to it. The ionic liquid-diffusion limits emerge in the thickest and most dense of cathodes, and requires a very low threshold voltage to be visible beyond the Ohmic/charge-transfer limit. The experimental data points to an optimal dense cathode thickness of 140 µm to 160 µm and our modeling suggests that the optimal thickness for cells with porous anodes would be much smaller. Overall, this work provides a broad and nuanced framework for understanding the design considerations in lithium-ion cells.

Acknowledgements

I would like to express my deep gratitude to my advisor and committee chair, Professor Jihui Yang, for his mentorship, patience, and continued support throughout my doctoral studies. His guidance and insight shaped not only this dissertation but also the way I approach research. I am especially grateful for the freedom he gave me to explore my own ideas while providing steady direction. I would also like to thank my committee members, Professors Jie, Jun, and David, for their thoughtful feedback and for helping shape this work to completion.

I am fortunate to have worked alongside an exceptional group of lab mates and colleagues. I thank Parker for keeping the laboratory running smoothly and for his dedication as chemical hygiene officer, as well as for his friendship over the years. I am grateful to Julia for countless discussions that clarified ideas, and to Mengyu, Lihua, and Xiaoyu for training me in the experimental procedures and crafts. I also appreciate the many friends and collaborators in neighboring labs and within the UW MSE community who contributed to the intellectual atmosphere that made this work possible. Support from the University of Washington, Battery500 Consortium, and the broader research community provided both resources and inspiration throughout this project.

Beyond the lab, I am grateful to my many close friends for providing balance, perspective, and much-needed breaks from research. Whether through long conversations, games of Magic: The Gathering, or evenings at the pub, their presence helped make this journey enjoyable and sustainable.

Finally, I would like to thank my wife, Sara, for her unwavering encouragement, patience, and belief in me throughout this process. Her support made the challenges of this degree possible to overcome. I am also deeply grateful to my family back home in Sweden for their constant love and encouragement, even from afar.

Contents

1. Introduction

(Note. Substantial portions of this work are taken verbatim from the manuscript titled On Rate-Limiting Mechanisms in NMC Cathodes: The Interplay of Low and High Current Constraints by Martin Brischetto, Sicen Yu, Jun Liu, Jie Xiao, and Jihui Yang published in Ref.[1].)

The transition from fossil fuels to renewable energy sources is one of the most pressing global challenges of the 21st century, and batteries are at the heart of this transformation. Among the various battery technologies available, lithium-ion batteries (LIBs) stand out due to their high energy and power density, making them particularly promising for a wide array of applications, most notably in electric vehicles (EVs). State-of-the-art, mass-produced, LIB packs used in EVs have energy densities ranging from $200\,\mathrm{Wh\,kg^{-1}}$ to $300\,\mathrm{Wh\,kg^{-1}}$, yet there is a constant push for improvements[2]. For instance, the Battery500 Consortium has set an ambitious target of developing LIB pouch cells capable of achieving energy densities of $500\,\mathrm{Wh\,kg^{-1}}$ with a cycle life of at least 1,000 cycles, thereby significantly enhancing the potential for mass EV adoption and extended use in renewable energy storage systems[3].

At the core of improving LIB performance lies the optimization of their components and design. A standard LIB consists of three primary active components: the anode, cathode, and electrolyte. The ability of a battery to store energy is largely determined by the selection and optimization of these active materials. However, the design of LIBs is constrained by the presence of several inactive components, such as separators and metal casings, which contribute to the overall mass without enhancing energy storage capacity[4]. These inactive materials represent a fixed cost in terms of weight, meaning that maximizing the proportion and utilization of active material within a given battery cell is key to improving energy density.

One avenue of research that has gained significant attention is increasing the loading of the cathode[5–8]. However, this strategy presents a significant trade-off; while increasing cathode loading can improve the battery's energy density, it simultaneously diminishes the rate performance, limiting the power density. A variety of studies have explored the rate-limiting mechanisms in cathodes, revealing that their rate performance is governed by several factors. During normal operation of a battery, at lower currents, the rate-limiting mechanism is determined by the nature of the active material, with $LiNi_{0.6}Mn_{0.2}Co_{0.2}O_2$ (NMC) cathodes limited by ionic solid-diffusion (ISD)[9–13] and $LiFePO_4$ (LFP) limited by phase transformation (PT)[14–16]. At higher currents, the rate-limiting mechanism is governed by Ohmic/charge-transfer (OCT) resistance[9,12,17,18], while in cathodes with higher loading it is governed by ionic liquid-diffusion (ILD)[9,12,19–21]. In addition to the electrochemical trade-offs, thick cathodes also suffer from cracking and delamination[8,22], prompting research into advanced fabrication techniques alleviating these issues[23–26]. These studies underscore the complexity of optimizing cathode design, as changes in thickness, porosity, tortuosity, and the inclusion of conductive carbon additives all affect the balance between energy density and power performance.

Much work has been put into describing and predicting how the rate-limits impact the rate performance of cells. Gallagher et al. developed a model predicting that the critical current is inversely proportional to cathode thickness, suggesting that ILD limitations are the primary cause of the sharp capacity drop at high discharge rates[20]. This model was expanded upon by Wang et al. to account for the distribution of dissolved lithium across the entire cell, including the anode and separator[21]. The concentration gradient in the electrolyte across the whole cell results in a reduced concentration in the cathode, suppressing ionic liquid-diffusion. This effect is most pronounced in cells where the cathode pore volume is small relative that of the separator and anode; e.g. in cells with porous anodes and/or thin cathodes. Interestingly, this means that, in terms of ionic liquid-diffusion, Li-metal anodes allow for much larger currents and/or cathodes than porous anodes do. However, Li-metal anodes have their own rate-limits related to the growth and structural integrity of the solid-electrolyte interphase (SEI) during stripping and plating[27–29], requiring high-performance electrolytes to form a more stable SEI[28,30]. In thin films and single particles, where ILD limits are absent, the capacity drops sharply at very high C-rates ($\gtrsim$100 C[10,11]) when the polarization pushes the knee of the discharge curve below the lower threshold voltage. The polarization is a function of cell resistance which, in turn, depends on cathode thickness, porosity, tortuosity, additives etc.[5,18].

Despite the substantial advancements made in understanding rate-limiting mechanisms, there remains considerable debate surrounding the identification and quantification of these factors based on rate performance data[10,20,31–40]. One of the key challenges lies in the similarity in the way different rate-limiting mechanisms manifest in rate performance data; with a sharp capacity drop at higher currents[35]. Although substantial data has been gathered and modeled to generate useful parameters for understanding these limits, some studies have not measured currents high enough to observe a pronounced capacity drop, which can cast doubt on certain conclusions about rate-limiting mechanisms[35]. Additionally, the occurrence of these limits within a relatively narrow current density range (typically 1 mA cm^{-2} to 10 mA cm^{-2}) across a broad spectrum of thicknesses (5 µm to 600 µm) compounds the difficulty of distinguishing between them[11,36]. Furthermore, the widespread use of C-rate rather than current density in evaluating rate performance can sometimes obscure the real physical effects, particularly when trying to isolate the impact of loading on performance[20,32,38].

To address these ongoing challenges, a more comprehensive approach is needed to better clarify the underlying mechanisms that limit rate performance. By improving our understanding of these factors, we can more accurately pinpoint the design parameters that need optimization to enhance battery performance. For example, if a cathode is found to be limited by Ohmic potentials, increasing conductivity–through additives such as carbon or by adjusting electrolyte and electrode properties–would be crucial. Conversely, if ionic liquid-diffusion is the primary limitation, adjustments in cathode porosity, tortuosity, thickness, or electrolyte diffusion characteristics may be necessary.

In this study, we aim to develop a more nuanced model that captures the relationship between rate-limiting mechanisms and rate performance data. We develop physics-based models describing the discharge dynamics in LFP and NMC cathodes and use these to an-

alyze galvanostatic rate performance data. We assemble NMC|Li-metal and LFP|Li-metal coin cells with cathodes of varying thicknesses and porosities, perform detailed rate performance measurements across a densely staggered set of discharge currents. This amounts to the largest, highest resolution, and highest quality rate performance data set available in literature[35,36]. We inspect the discharge curves and rate performance data and use our models to identify the governing rate-limiting mechanisms and the capacity drop current. We use the models to predict the optimum cathode thickness at a given operating current. We investigate the trade-off in the LFP discharge between the number of participating particles and their average transformation current. Furthermore, we investigate the interplay between the various rate-limits by analyzing the discharge curves at different lower threshold voltages, allowing us to better understand how the mechanisms interact under varying operating conditions. This comprehensive approach will provide clearer insights into optimizing LIB cathodes for high-energy applications without compromising rate performance, ultimately contributing to the broader effort of improving battery technologies for future energy needs. This dissertation begins with an in-depth description of the discharge process in NMC and LFP cathodes and the mechanisms that lead to the underutilization of capacity. The next section outlines how we assemble our coin cells, calculate the porosity of their cathodes, and the rate performance program we put them through. After methods, we use simulations of NMC cathodes to tie features in the experimental discharge curves and rate performance data to physical events in the cathode. We use these insights to identify the rate-limiting mechanisms in our experimental data. The subsequent analysis is divided into two parts. First we treat the rate-limits at low currents; ISD in NMC and PT in LFP. Second, we analyze the rate-limits at high currents that cause the sharp capacity drop; ILD and OCT. Finally, we summarize our conclusions.

2. Background: Discharge Dynamics

A LIB consists of, at minimum, an anode in which lithium has a high electrochemical potential and a cathode in which lithium has a low electrochemical potential, connected into a circuit through an ion conductor (the electrolyte) and an electron conductor (external wiring). During discharge, lithium ions spontaneously dissolve into the electrolyte at the anode and, at the same time, lithium ions are spontaneously intercalated into the active material in the cathode. The resulting concentration gradient in the electrolyte causes the dissolved lithium to diffuse from the anode, across the separator, into the cathode.

During a *galvanostatic* discharge, a counteracting voltage is applied to maintain a constant cell current. Simulations show that the process quickly reaches a quasi-steady-state wherein the cathode active material is filled, the anode active material is depleted, and the concentration gradient in the electrolyte is slowly evolving[21,41]. The applied voltage measured through a galvanostatic discharge is one of the most basic properties of an operating battery. But in order to understand what the discharge curve tells us about the battery, we must consider the process evolving between the current collectors. The nature of this process depends on the nature of the active materials. Figure 2 illustrates the difference between LFP cathodes and NMC cathodes.

NMC cathode particles are relatively large (∼10 µm) spherical agglomerations of small primary particles. The material is a *layered transition metal oxide* wherein covalent layers of O–[Ni|Mn|Co]–O are stacked, separated both by weak Van-der-Waals forces and by small lithium ions loosely bound between the layers[42]. In the discharged state, NMC has a lithium ion for every two oxygen atoms. When charging, the lithium is pulled out by applying a voltage greater than ∼3.7 V vs Li/Li^+ (μ_{NMC}^{max} in Figures 2a and d). The equilibrium voltage increases as more lithium is pulled out. At 4.2 V (μ_{NMC}^{min} in Figures 2a and d), NMC has ∼42 % of the lithium compared to that in the discharged state. The relationship between the equilibrium voltage and the filling fraction, $\mu_{NMC}(c_s)$, is shown in Figure 2d with a black dotted line. When excessive amounts of lithium are pulled out, the layered structure deteriorates and the oxygen is released, reducing the capacity of the material[43].

During a galvanostatic discharge, a voltage just below the equilibrium voltage is applied, causing the lithium ions dissolved in the electrolyte to intercalate into the NMC. The applied voltage must continuously decrease in order to maintain the constant cell current as the particle surface is filled and its chemical potential increases. Simulations show that the cell current is distributed across the cathode in discharges of NMC (see Section 4). This is because the reaction rate at an NMC surface, j, depends on both the lithium-ion concentration and the electrochemical potential in the electrolyte and the particle surface. This relationship can be understood in terms of the Butler-Volmer equation.

$$\begin{aligned} j &= j_0 \left(\exp\left[-\frac{\alpha F \Delta\overline{\mu}}{RT} \right] - \exp\left[\frac{(1-\alpha) F \Delta\overline{\mu}}{RT} \right] \right) \\ j_0 &= k_0 \left(\frac{c_{el}}{c_{el,0}} \right)^{1-\alpha} \left(\frac{c_{s,surf}}{c_{s,max}} \right)^{1-\alpha} \left(1 - \frac{c_{s,surf}}{c_{s,max}} \right)^{\alpha} \\ \Delta\overline{\mu} &= \overline{\mu}_{el}(c_{el}) - \overline{\mu}_s(c_{s,surf}) \end{aligned} \tag{1}$$

where α, RT/F, $\Delta\overline{\mu}$, $\overline{\mu}_{el}$, $\overline{\mu}_s$ is the charge transfer coefficient, the thermal voltage, the cathode surface overpotential, and the electrochemical potentials of the electrolyte (teal solid and dashed lines in Figure 2a and b) and solid (orange solid and dashed lines in Figure 2a and b). The exchange current density, j_0, is a function of the lithium-ion concentration in the electrolyte c_{el} and at the particle surface $c_{s,surf}$, and material constants like the maximum particle concentration $c_{s,max}$, rate constant k_0, and reference electrolyte concentration $c_{el,0}$. Both the exchange current density and the cathode surface overpotential, and consequently the reaction rate, decreases as the particle surfaces fill. This has a homogenizing effect on the reaction rate across the cathode, as it impedes the reaction at surfaces that are further along while accelerating the reaction at surfaces that lag behind. Although, the gradient in the electrochemical potential of the electrolyte has the opposite effect, as it promotes a higher reaction rate closer to the separator. Once the first NMC surfaces become fully filled (t_2 and dashed lines in Figures 2b and d), the applied voltage drops sharply in order to maintain the constant current, increasing the surface overpotential at the remaining NMC surfaces. This kicks off a spiral of an accelerating voltage drop

as more particle surfaces fill. Soon thereafter, the threshold voltage is reached, ending the galvanostic discharge. This means that the diverging voltage primarily tells us something about the solid-diffusion properties of the active material and the homogeneity of the cathode reaction rate. For instance, slow solid diffusion results in the surfaces filling up much quicker than the particle as a whole, resulting in the voltage diverging early. Additionally, a very homogeneous reaction rate results in a sharp voltage drop, as all particle surfaces reach full filling simultaneously. We refer to this mechanism as the ISD rate-limiting mechanism, and it is what determines the capacity utilization at low currents. In section 5.1, we develop a simple model to predict the relationship between discharge current and capacity utilization in an ISD limited discharge. We then use this relationship to identify the discharge currents at which NMC|Li-metal leaves the ISD rate-limited regime.

Unlike in NMC cathodes, the discharge process of an LFP cathode is very non-uniform [1,21]. LFP-particles transform one-by-one, where individual particles may transform at 3–4 C while the cathode as a whole dis/charges at 0.5–2 C [15,44,45]. This is caused by the phase-change mechanism by which the transformation occurs. LFP is stable at lithium concentrations below 5 % and above 90 % [46]. In between, LFP particles form high- and low-concentration phases, separated by a narrow phase boundary. These phases take hours to form [15]. While transforming however, the particle transforms like a solid-solution, through a high potential transition phase [15,44,47]. In a collection of particles, this results in the preferential transformation of those particles which have already begun transformation [48,49]. However, LFP has been shown to reach a maximum transformation rate of about 14.2 C [16]. Thus, at the cell level, in a galvanostatic discharge the reaction is limited to a narrow reaction zone (shaded region in Figure 2a) in the yet-to-be-transformed region traversing the cathode from the separator to the current collector [21]. At some time t_2, the reaction zone reaches the current collector and the number of untransformed particles becomes limiting, causing the applied voltage to diverge in order to increase the overpotential and maintain the constant current (see black line in Figure 2c). A large reaction zone results in the voltage diverging earlier and an average reaction zone C-rate close to the maximum C-rate results in a sharp voltage drop, as the diverging voltage is not able to increase the local C-rates. We call this the phase-transformation rate-limiting mechanism (PT), as the discharge capacity is limited by the transformation rate of the particles. This is the relevant rate-limiting mechanism at low currents and in low-capacity cells. It's difficult to observe this trade-off in an operating battery. However, time t_2 is a moment where we know both the amount of LFP participating in the discharge (the remaining capacity) and what current they're collectively delivering (the cell current), providing us with an indication of their relationship. In section 5.2, we develop a simple model to extract the average reaction zone C-rate from the galvanostatic discharge curves. We then extrapolate its relationship to the cell current to find the current beyond which the full cathode is required to deliver the cell current right from the start of discharge. We call this current the phase-transformation critical current I_{crit}^{PT}.

In both NMC and LFP, the driving force of the discharge process are the overpotentials at the anode and cathode. A larger discharge current requires larger overpotentials and results in steeper electrochemical gradients in the electrolyte. We refer to the sum of these

potentials as the Ohmic/charge-transfer voltage ΔV_{OCT}, indicated by dashed and solid arrows in Figure 2.

$$\Delta V_{OCT} = \eta_{an} + \Delta\overline{\mu}_{el} + \Delta\overline{\mu} + \Delta\overline{\mu}_s \tag{2}$$

where η_{an} is the surface overpotential at the metal anode surface (indicated with arrows for t_1 in Figures 2a and b); $\Delta\overline{\mu}_{el}$ and $\Delta\overline{\mu}_s$ are the changes in electrochemical potential difference along an arbitrary path from the lithium metal anode, across the electrolyte to a reaction location, and from the reaction location across the conductive matrix of the cathode, respectively (orange and teal lines in Figures 2a and b, solid lines for t_1 and dashed for t_2); and $\Delta\overline{\mu}$ is the difference in electrochemical potential between the electrolyte and the active particles at the reaction location. These can be expressed as

$$\begin{aligned}\Delta\overline{\mu}_{el} &= \overline{\mu}_{el,an} - \overline{\mu}_{el},\\ \Delta\overline{\mu} &= \overline{\mu}_{el} - \overline{\mu}_s, \text{ and}\\ \Delta\overline{\mu}_s &= \overline{\mu}_s - \overline{\mu}_{s,cat}\end{aligned}$$

where $\overline{\mu}_{el}$ and $\overline{\mu}_s$ are the electrochemical potentials of the electrolyte and the active material, and where the indices *an* and *cat* represent their values at the anode and cathode current collectors, respectively. At large enough currents, the OCT voltage becomes large enough that the applied voltage reaches the threshold voltage before the ISD or PT limits are reached. This can be identified on a discharge curve by the absence of a diverging voltage at the end of discharge. We call this voltage limit the margin voltage, ΔV_{margin}, and is the voltage difference between the equilibrium potential at full filling and the threshold voltage, indicated with an arrow to the right in Figures 2c and d. The discharge current beyond which $\Delta V_{OCT} \geq \Delta V_{margin}$ is the OCT critical current, I_{crit}^{OCT}. Discharge currents beyond this current result in severe underutilization of the cell capacity. In Section 6.2, we derive expressions for the ΔV_{OCT} as function of cell current. In addition, we measure ΔV_{OCT} in NMC|Li-metal and LFP|Li-metal cells with varying cathode thicknesses and porosities across a series of galvanostatic discharge currents. These are used to compare the extrapolated I_{crit}^{OCT} with the current at the sharp capacity drops identified as OCT, I_{drop}^{OCT}. In Section 6.2.3, we show how the choice of the margin voltage impacts the observed rate-limiting regimes.

If the lower threshold voltage is set low and the cathode is thick and dense, the discharge becomes limited by ionic liquid-diffusion. This occurs when the electrolyte is depleted faster than it can be replenished through ionic liquid-diffusion, making the active particles in the deepest section of the cathode inaccessible. The applied voltage diverges as soon as the accessible active particles are filled, but unlike the PT and ISD rate-limiting mechanisms, the ILD mechanism also results in a sharp capacity drop. In Section 6.1, we develop simple descriptions of the concentration profiles across uniform reaction (UR) and (MZR) anodes ILD and cathodes. We use these to calculate the critical current, I_{crit}^{ILD}, at which the electrolyte is depleted at any location in the cathode. We find that the UR|Li-metal type cells allow for the largest cathodes, while UR|UR type cells are the most prone to ILD limits. In Section 4, simulations are used to further illustrate the ISD, ILD, and OCT rate-limiting mechanisms and the origins of the resulting capacity underutilization.

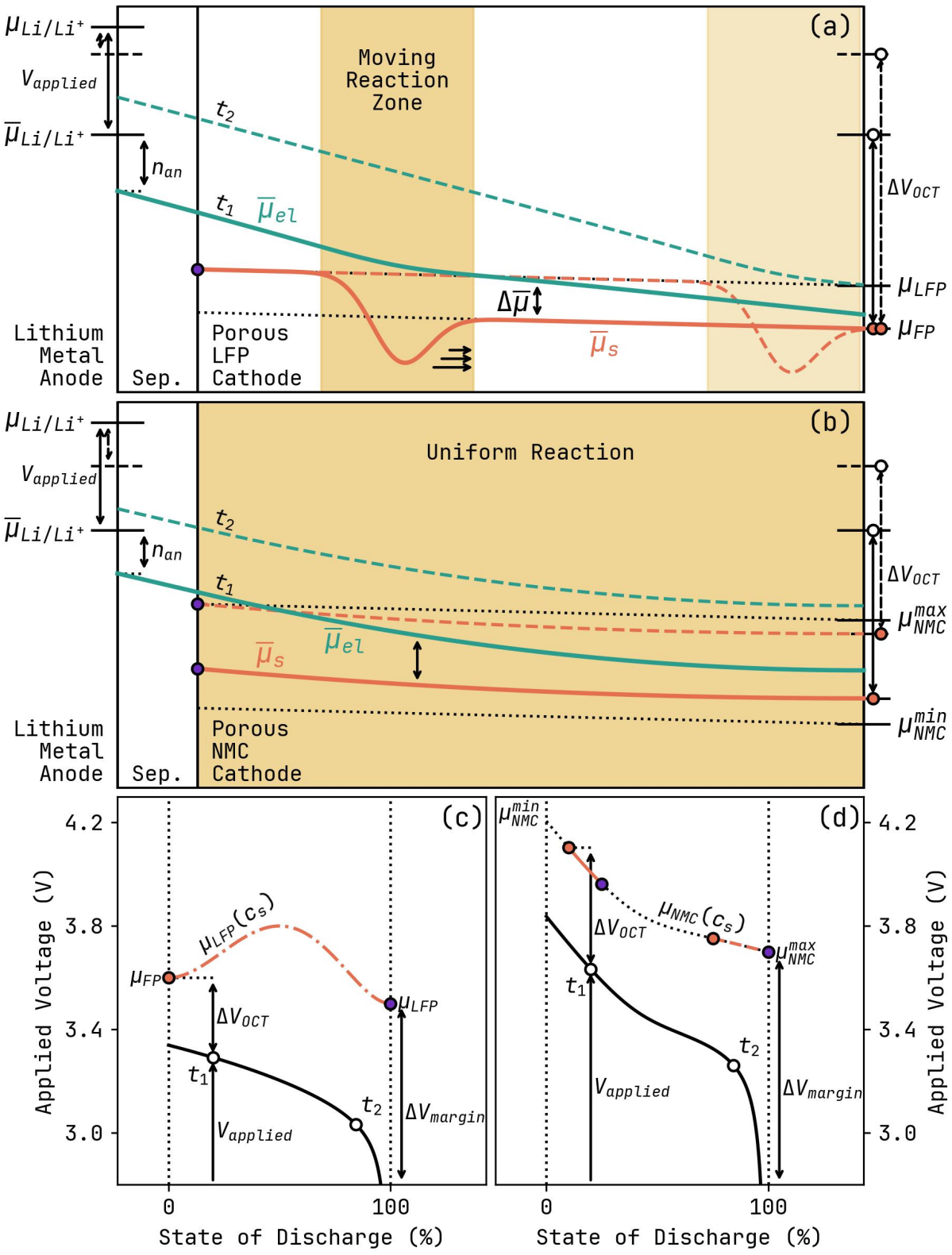

(Caption on next page.)

Figure 1: Discharge Dynamics and Cell Voltage. Figures (a) and (b) are schematic cross sections of (a) an LFP|Li-metal cell and (b) an NMC|Li-metal cell, illustrating the Moving Zone Reaction and Uniform Reaction Discharge Modes, respectively. The electrochemical potential of the Li-metal, $\overline{\mu}_{Li/Li^+}$ (marked with a horizontal solid and dashed line to the left), is the sum of its chemical potential, μ_{Li/Li^+} (horizontal line at top left), and the electrostatic potential supplied by the applied voltage Vapplied (indicated with an arrow the left, solid for t_1 and dashed for t_2). The driving force for the dissolution of Li^+ is the anode surface overpotential, η_{an}, indicated with an arrow for t_1. The colored lines represent the electrochemical potential of lithium in the electrolyte, μ_{el}, (teal) and in the active material, μ_s, (orange) at an early time t_1 (solid lines) and just before the end of discharge t_2 (dashed lines). The driving force of the intercalation of lithium into the cathode active material is the electrochemical potential difference between the electrochemical potentials in the electrolyte and active material, $\Delta\overline{\mu}$, marked with an arrow. The dotted lines mark the electrochemical potentials of (a) LFP at full filling, μ_{LFP}, and at minimal filling μ_{FP}; and (b) NMC at full filling, μ_{NMC}^{max}, and at the charged equilibrium voltage, μ_{NMC}^{min}. The slight slope represents the Ohmic potential in the solid phase. The yellow shading shows the reaction zone, indicating a uniform reaction in NMC (b) and a narrow moving reaction zone in LFP (a) at time t_1 (left shaded zone) and t_2 (right shaded zone). The sum of all overpotentials and gradients across the cell is the OCT voltage, ΔV_{OCT} (indicated with an arrow to the right, solid for t_1 and dashed for t_2). Figures (c) and (d) illustrate the potentials as they relate to the galvanostatic discharge curves for (c) LFP and (d) NMC. The black solid line represents the discharge curve, $V_{applied}$ vs State of Discharge. The white circles mark the times t_1 and t_2 illustrated in (a) and (b). The equilibrium voltage of the two materials, $\mu_{LFP}(c_s)$ and $\mu_{NMc}(c_s)$, are represented with an orange dash-dot line in (c) and a black dotted line in (d). In LFP, the individual particles must transform through an energy barrier and do so one-by-one, while in NMC the chemical potential decreases continuously with state of discharge. The orange and purple circles mark the chemical potential of the solid phase at the cathode current collector and at the cathode/separator-interface, respectively. In (d), orange solid and dashed lines mark the range of chemical potentials at the NMC particle surfaces in (b) at times t_1 and t_2, respectively. ΔV_{OCT}, indicated with an arrow for time t_1, is the electrochemical potential difference between the equilibrium voltage for the concentration at the cathode current collector, $\mu_{NMC}(c_{s,cc})$, and the applied voltage $V_{applied}$. The margin voltage ΔV_{margin}, indicated with arrows in (c) and (d), represents the upper limit for ΔV_{OCT} beyond which the discharge becomes OCT-limited.

3. Methods

3.1. Cell Assembly

NMC and LFP cathode films coated on aluminum foil were purchased from NEI corporation. The cathodes were received lightly calendered and had 5 different active mass

loading. The NMC films consisted of 90 wt.% NMC, 5 wt.% conductive carbon (Super P), and 5 wt.% polyvinylidene fluoride (PVDF). The LFP films consisted of 88 wt.% LFP, 7 wt.% Super P, and 5 wt.% PVDF. The cathode sheets arrived with a porosity of roughly 50 %. Two additional batches of cathode discs were prepared by calendering two sets of cathode sheets to porosities of roughly 27 % and 19 %. Four 1/2 inch diameter discs were punched out of each sheet and dried overnight at 120 °C in a vacuum oven before being transferred into a glove box with an Argon atmosphere. Localized high concentration electrolyte (LHCE) was prepared by mixing lithium bis(fluorosulfonyl)imide (LiFSI, Nippon Shokubai), Dimethoxyethane (DME, Gotion), and 1,1,2,2-tetrafluoroethylene 2,2,3,3-tetrafluoropropyl ether (TTE, Synquest) in a molar ratio of 1:1.2:3. Each coin cell was assembled with an Aluminum-clad stainless steel cathode case (MSE Supplies), an additional layer of Aluminum foil, a cathode disc, a 16 µm PE separator (Nanoshel), 60 µL electrolyte, a 250 µm Li-metal chip (MSE supplies), a 1 mm stainless steel spacer (MSE Supplies), a stainless steel spring (MSE Supplies), and a stainless steel anode case (MSE Supplies). The cell stack was subsequently crimped at 50 kg cm^{-2} pressure with an MSK-110 Hydraulic Crimping Machine (MTI) and then left to rest for at least 24h.

3.2. Cathode Thickness and Porosity

As each cathode was punched out of the larger calendered sheet, their masses were weighed and their thicknesses were measured with a caliper. The film porosity was calculated for each cathode using

$$\varepsilon = 1 - \frac{\rho_{cat}}{\rho_s} \tag{3}$$

where ρ_{cat} and ρ_s are the geometric density and density of the solid phase of the cathode film, respectively. ρ_{cat} is calculated with

$$\rho_{cat} = \frac{M_{cat}}{AL_{cat}} \tag{4}$$

where M_{cat}, A, and L_{cat} are the cathode film mass (disc mass minus the foil mass of 4.14 mg cm^{-2}), the disc area, and the film thickness (disc thickness minus the foil thickness of 17 µm). ρ_s is calculated with

$$\frac{1}{\rho_s} = \frac{w_{NMC}}{\rho_{NMC}} + \frac{w_{PVDF}}{\rho_{PVDF}} + \frac{w_{carbon}}{\rho_{carbon}} \tag{5}$$

where w_i and ρ_i are the mass ratio and density of component i. The densities of NMC, Super P, and PVDF are 4.44 g cm^{-3}, 1.6 g cm^{-3}, and 1.78 g cm^{-3}, respectively, resulting in a solid phase density of 3.82 g cm^{-3}. The measured active material loadings, porosities, and nominal capacities are summarized in Tables 3 and 4 in Appendix D.1.

3.3. Rate Performance Experiment

All cycles start with the same charging step: (1) charge at C/10 until cell voltage reaches the upper threshold voltage (3.8 V for LFP, 4.2 V for NMC), (2) hold the applied voltage

until current decreases to C/200, (3) 1 h rest. The first three formation cycles define 1 C as $160\,\mathrm{mA\,g^{-1}}$ for LFP and $177\,\mathrm{mA\,g^{-1}}$ for NMC. Subsequent cycles define the C-rate based on the discharge capacity at the end of the formation cycles. After charging, the cell is discharged at a constant current to 2.0 V. Each cycling condition was repeated three times. The experiment goes through three phases:

1. Formation Cycles:
   (a) The cell is discharged at C/10
   (b) Record the discharge capacity of the third formation cycle, Q_{nom}
2. Rate performance (i starts at 0):
   (a) The cell is discharged at $(1\,\mathrm{mA\,cm^{-2}})\cdot 1.15^i$
   (b) Record the discharge capacity of the third cycle, Q_i
   (c) if $Q_i < 0.05 Q_{nom}$, move on to the final phase, otherwise increase i by 1 and repeat.
3. Final Cycles:
   (a) The cell is discharged at C/10

The cycling program results in the cells being cycled 60–100 cycles, many of which at relatively high currents. An LHCE was chosen as the electrolyte in order to limit the strain on the Li-metal anode. LHCEs have exceptional stability against Li-metal, in particular at higher currents[28,30]. In addition, the upper threshold voltage was limited to 4.2 V, which is significantly below the stability limit of the electrolyte[30].

4. Simulating Rate-Limiting Mechanisms in NMC|Li-metal cells

Pseudo two-dimensional simulations based on Porous Electrode Theory[50] were performed to gain a better understanding of how rate-limiting mechanisms are impacted by cathode thickness. We used the open-source software package MPET developed by Smith et al.[41]. The details of the model are explained in Appendix A. Figure 2 shows the result of simulations where three NMC|Li-metal cells were galvanostatically discharged from 4.2 V to 2.5 V in a densely staggered series of discharge currents. We use these to illustrate how the rate-limiting mechanism is interpreted from the discharge curves (see Figure 2a and b) and rate performance data (see Figure 2f and g).

Figures 2a and b shows the applied voltage throughout each discharge for two cells with 200 µm and 50 µm cathodes, respectively. Each line represents one discharge, with those discharge curves reaching the higher voltages and capacities resulting from lower discharge currents. Each current is 15 % larger than the previous, like in our experiments. The discharge capacity of these discharges are shown in Figures 2f and g, in addition to those of a cell with a 100 µm cathode, in units of $\mathrm{mAh\,cm^{-2}}$ vs. $\mathrm{mA\,cm^{-2}}$ and $\mathrm{mAh\,g^{-1}}$ vs. $\mathrm{h^{-1}}$, respectively. Figures 2c,d, and e show the cross-sections of the simulated distribution of lithium at the moment when the applied voltage reaches the threshold voltage, for a

selection of discharges (marked with open markers in Figures 2f and g). The solid black line represents the lithium concentration at the surface of the NMC particles; the dashed black line represents the average particle concentration; and the blue line represents the concentration of lithium dissolved in the electrolyte. Figure 2c shows the end of an ISD limited discharge (red), defined as one where all particle surface are full at the end of discharge. Figure 2d shows the end of an ILD limited discharge (blue), defined as one where the electrolyte is depleted at any point in the cathode. Figure 2d shows the end of an OCT limited discharge (yellow), defined as one where none of the surfaces are full at the end of discharge.

We see that, at low currents, the discharge is ISD limited and its capacity decreases slowly with discharge current. At higher currents, the capacity drops as the discharges enter the ILD or OCT regimes. In the simulations, there is a difference in how sharp the capacity drop is as the current enters the ILD and OCT regimes. This difference is not observed in our experimental data; all sharp capacity drops are roughly equally sharp. Instead, we look at the difference between the OCT (yellow lines) and ILD (blue lines) discharge curves in Figures 2a and b. The OCT limited discharges end before the applied voltage diverges, while in ILD limited discharges the voltage diverges. This is how the rate-limiting mechanisms are identified. Although LFP cells are not included in Figure 2, the OCT and ILD rate-limiting mechanisms work similarly and we use the same method to identify the mechanisms, with the exception that the mechanism at low currents is assumed to be PT rather than ISD.

The discharge curves, rate performance, and critical currents of all 86 LFP|Li-metal coin cells and 58 NMC|Li-metal coin cells are shown in Figures 13A-D in Appendix D.2.

5. Rate-Limits at Low Currents

At low currents, the behavior of active material particles matter more than the design of the cathode film. As discussed in Section 2, the LFP and NMC active particles discharge in with different processes and consequently, their underutilization depends on different mechanisms. In this section, we develop physics-based models describing the capacity loss at the cathode level given the two different mechanisms. In NMC, the model is used as a baseline to identify the ILD and OCT critical currents. In LFP, the model is used to predict the PT critical current, beyond which the cell discharge capacity drops sharply due to phase-transformation limits.

5.1. Ionic Solid-Diffusion Rate-Limit in NMC Cathodes

An ISD-limited discharge is one that finishes in a state of full surface filling ($c_{s,surf} = c_{s,max}$). The distribution of lithium at the end of an ISD-limited discharge is shown in Figure 2c. The surface filling (solid black line) is maximized throughout the cathode. Due to the time it takes for lithium to diffuse from the particle surface to the center, the average particle filling (black dashed line) is always lower than that at the surface. This difference between surface and average filling represents an underutilized capacity.

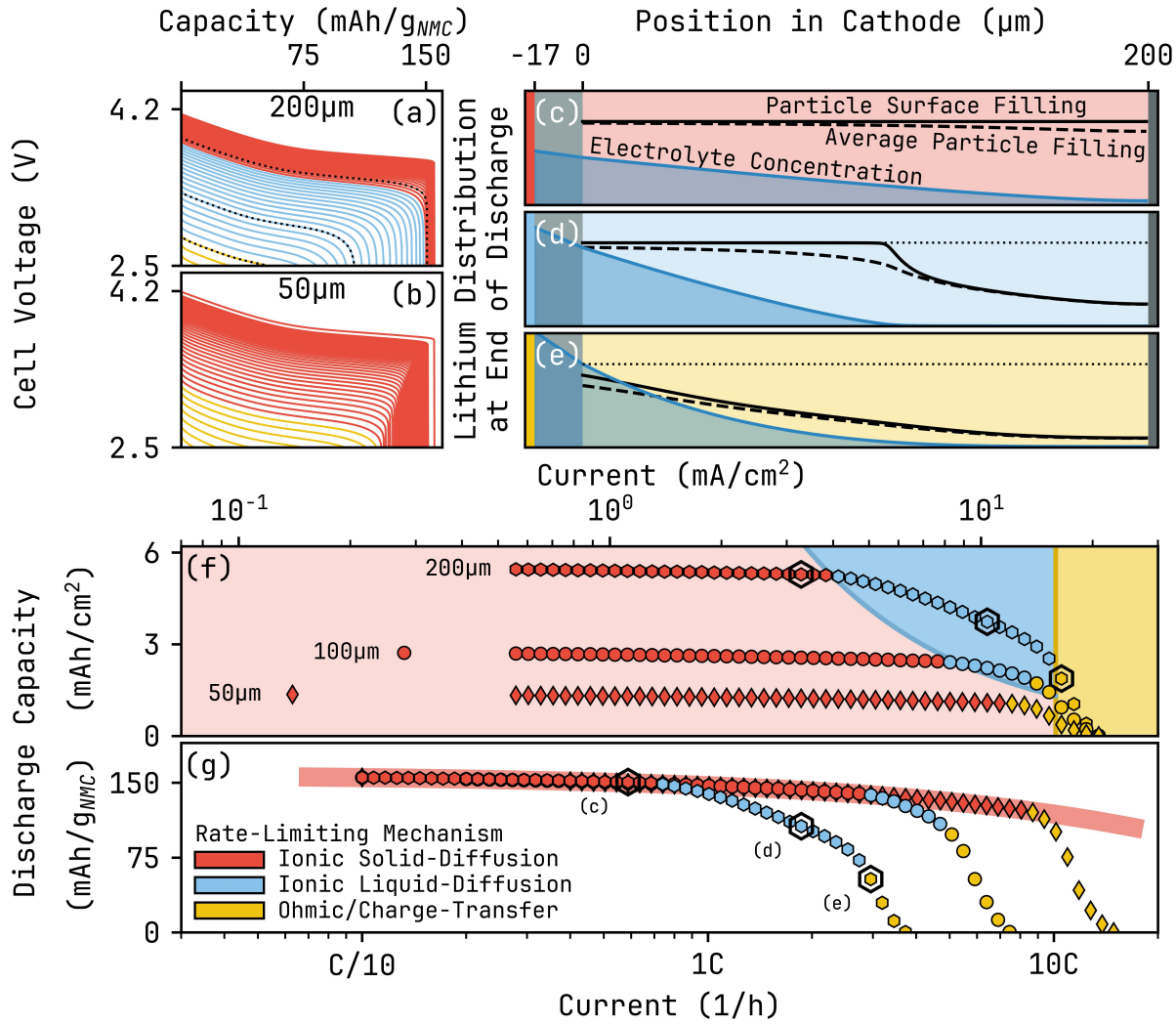

Figure 2: Results from simulations of discharges of NMC|Li-metal cells with cathode thicknesses of 50 µm, 100 µm, and 200 µm. (a-b) show the simulated discharge curves of cells with 200 µm and 50 µm cathodes, respectively. (c-e) shows the distribution of lithium at the end of (c) an ISD-limited discharge, (d) an ILD-limited discharge, and (e) an OCT-limited discharge. (f-g) show the rate performance of the cells in units of mAh cm^{-2} vs. mAh cm^{-2} and mAh g^{-1} vs. h^{-1}, respectively. The discharges in (c-e) correspond to the discharges marked in (f-g) with open black hexagons and in (a) with dotted lines. The colors of the markers in (f-g), lines in (a-b), and backgrounds in (c-e) are defined by the complete (red), partial (blue) and no (yellow) particle surface filling at end of discharge.

Its magnitude is determined by the flux of lithium across the particle surface and the rate of ionic diffusion within the particle. Higher discharge currents means that less lithium has entered the particle by the time the surface is full. The specific discharge capacity of the different cathodes in this region aligns closely, independent of cathode geometry (see red diamonds, circles, and hexagons in Figure 2g). This suggests that the mechanism is mostly independent of cathode geometry and depends mainly on parameters related to solid diffusion. Based on this understanding, a simple model is developed in Appendix B to fit the experimental data in the low-current region.

$$\frac{Q}{M} = Q_M\big(1 - (\tau R)^n\big) \tag{6}$$

τ represents the time constant of diffusion in the active particle, given the particle shape/size distribution and diffusion coefficient. n represents the deviation from a constant solid-diffusion coefficient model. Equation 6 resembles the rate fitting equation developed in refs.[35,51]. In contrast, however, Equation 6 only applies in the low-current region, decoupling the low-current region from the other regions. This allows us to create a common baseline for all cathodes made from the same active material powder (with similar solid-diffusion properties) to compare other effects against. The understanding that the ISD limited region occurs at currents below the critical current runs counter to some previous analyses[10,52]. However, the sharp capacity drop in rate performance measurements of single particles or thin films, where solid diffusion is emphasized, often occurs at very high C-rates ($\gtrsim$100 C[10,11], $\gtrsim$7.6 mA cm^{-2} [11]), and are arguably caused by OCT limits.

Figure 3a shows the specific capacity of NMC|Li-metal coin cells with a range of cathode thicknesses and porosities of $\sim$51 %, discharged in a series of discharge currents. The specific capacity is $\sim$150 mAh g^{-1} when discharged at C/10. As the C-rate increases, the capacity decays slowly until there is a sharp capacity drop. All cathodes follow the same capacity decay at low currents, while the sharp capacity drop occurs at lower C-rates as the cathode thickness increases. This general behavior matches that of the simulations in Figure 2g. In order to investigate the rate-limits that cause the sharp capacity drop, we need a common and consistent definition of the critical current. We fit Equation 6 to the low current data of all 20 cells collectively. The ISD-limited data is marked with red markers and the resulting fit is shown in Figure 3a with a wide red semi-transparent line. This line is used as a baseline and the critical current (blue diamonds in Figures 3a and b) is defined as the current where the data falls below 90 % of this line (red dashed line in Figure 3a).

Figure 3b shows the critical currents of the cathodes in Figure 3a. We see that the critical current in the thick cathodes ($\gtrsim$100 µm) follows an inverse-power relationship ($I_{crit} \propto L_{cat}^{-1.06}$), matching that predicted for ILD-limits[20]. In the thinner cathodes, on the other hand, the critical current decays much more slowly ($I_{crit} \propto L_{cat}^{-0.31}$). This suggests that the sharp capacity drop in the thinner cathodes is caused by rate-limits other than ILD. In the following section, we will show that these are caused by the OCT-limit.

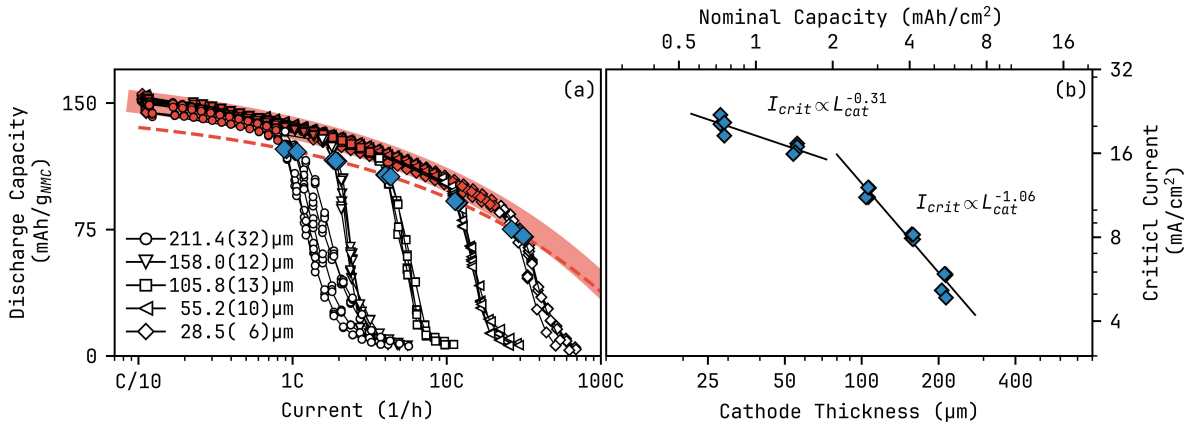

Figure 3: Experimental rate performance data (a) and critical currents (b) of NMC|Li coin cells, with a range of cathode thicknesses, discharged over a series of current densities. The wide semi-transparent red line in (a) represents the ISD-limited capacity. The red dashed line in (a) marks 90 % of the ISD-limited capacity, used to define the critical current. The upper axis in (b) shows the nominal capacity based on the average volumetric capacity of all cathodes. Note that (b) is a log-log plot. 1 C is defined from the discharge capacity of the formation cycles.

5.2. Phase-Transformation Rate-Limit in LFP Cathodes

LFP particles have a limited transformation rate[16,48,49]. This means that the current must be distributed across many particles within a volume. The transformation rate of LFP is described well by Marcus-Hush-Chidsey theory, wherein the reaction rate plateaus at high overpotentials[16]. In 2014, Bai et al. measured the reaction rates of LFP in 5 µm porous films using chronoamperometry[16]. They found an asymptotic C-rate of 14.2 C that was reached at an overpotential of ∼411 mV. In a galvanostatic discharge of a thick cathode at lower currents, there is a trade-off between the activation energy of untransformed particles and the insertion energy of actively transforming particles[48]. This trade-off determines the size of the reaction zone and the reaction rates of the particles. If the cell current I is generated entirely within the reaction zone, it can be expressed with equation 7, shown below.

$$I = (1 - \varepsilon_{cat}) Q_{V,s} \Delta x_r \bar{r} \tag{7}$$

where $Q_{V,s}$ is the volumetric capacity of the solid phase of the porous cathode, Δx_r is the reaction zone width, and $\bar{r}$ is the average C-rate of the LFP particles in the reaction zone. The average reaction rate in the reaction zone can be estimated from the discharge curve. The voltage drop at end of discharge corresponds to the moment when the number of not-yet-activated particles in the cathode is depleted. At this point, all remaining particles are participating in the discharge and the average C-rate can be estimated with equation

8, shown below

$$\bar{r} = \frac{I}{Q_A - Q_{drop}} \tag{8}$$

where Q_A is the nominal areal capacity and Q_{drop} is the discharged capacity when the voltage drops. Given that the total current is the product of the number of participating particles and their average C-rate ($I \propto \bar{r}\Delta x_r$), fitting the reaction zone C-rate to a power-law ($\bar{r} = aI^b$) reveals the trade-off between the increases in the two. $b = 1$ corresponds to a constant number of participating particles, while $b = 0$ corresponds to a constant local C-rate. The critical current, I_{crit}^{PT}, is the current beyond which the full cathode is participating in the discharge. This current can be estimated by extrapolating equation 7, inserting $\Delta x_r = L_{cat}$ and $\bar{r} = aI^b$, and solving for the critical current, shown below.

$$I_{crit}^{PT} = (a(1 - \varepsilon_{cat})Q_{V,s}L_{cat})^{\frac{1}{1-b}} = (aQ_A)^{\frac{1}{1-b}} \tag{9}$$

At discharge currents beyond this current, the overpotential grows larger until the particles are transforming at their maximum transformation rate, reaching the maximum cell current $I_{max} = Q_A r_{max}$. We can gain some insight into the trade-off between $\bar{r}$ and Δx_r by finding the average C-rate of the participating particles just as the voltage starts to diverge. This is the moment when all remaining particles are participating in the discharge. Knowing how this trade-off evolves with cell current allows us to find the critical current, I_{crit}^{PT}, beyond which the discharge starts out with the cell voltage immediately diverging as the particles are transformed.

Figure 4a-c shows the discharge curves of three LFP|Li-metal coin cells with thin $0.58\,\mathrm{mAh\,cm^{-2}}$ cathodes calendered to different porosities, discharged over a series of currents. The markers show the location where the voltage diverges. This point is defined as the time at which the voltage drops more than 100 mV below the linear extrapolation of the plateau. This extrapolation is based on the linear fit used for the analysis of the OCT limit in Section 6.2. Figure 4d shows $\bar{r}$ (see equation 8) extracted from Figures 4a-c plotted against discharge current I. We fit a power-law to each of the data sets. The $\sim$C/10 formation cycles and final cycles (gray and open markers, respectively) are excluded from these fits due to the large spread at low currents. At higher currents, the data fits the power-law very well and is mostly independent of the degree of calendering. Figure 4e shows the specific discharge capacity of the three coin cells against discharge current. The vertical solid lines show the I_{crit}^{PT} calculated with equation 9. The critical current of the most dense cathode (blue solid line) matches the location of its sharp capacity drop at around 40 C. This drop is caused by the phase-transformation limits of the LFP particles. In contrast, critical currents of the two more porous cathodes (yellow and red solid lines) are far above their respective sharp capacity drop. These capacity drops instead match the OCT critical currents (vertical dotted lines). Inspecting the discharge curves, we see that the capacity drop of two more porous cathodes correspond to OCT limited discharges.

The exponents b of the fits from all 86 coin cells are plotted against cathode thickness in Figure 4f. Each marker in 4f represents the average power-law exponent among 3-4 identical coin cells and the error bar represents their standard deviation. The cells have an

average exponent of roughly $\bar{b} = 0.552(94)$ that decreases with thickness and density. This indicates that both the local C-rate and the number of participating particles increase by roughly the square root of cell current. Figure 4g shows the coefficient a of the fits from all cells. a corresponds to the average reaction zone C-rate at cell current of $1\,\mathrm{mA\,cm^{-2}}$ and ranges from 6 C in the most dense and thin cathodes to 2 C in the most porous and thick cathodes. This means that that thicker, more porous, cathodes distributes the cell current across a larger number of particles.

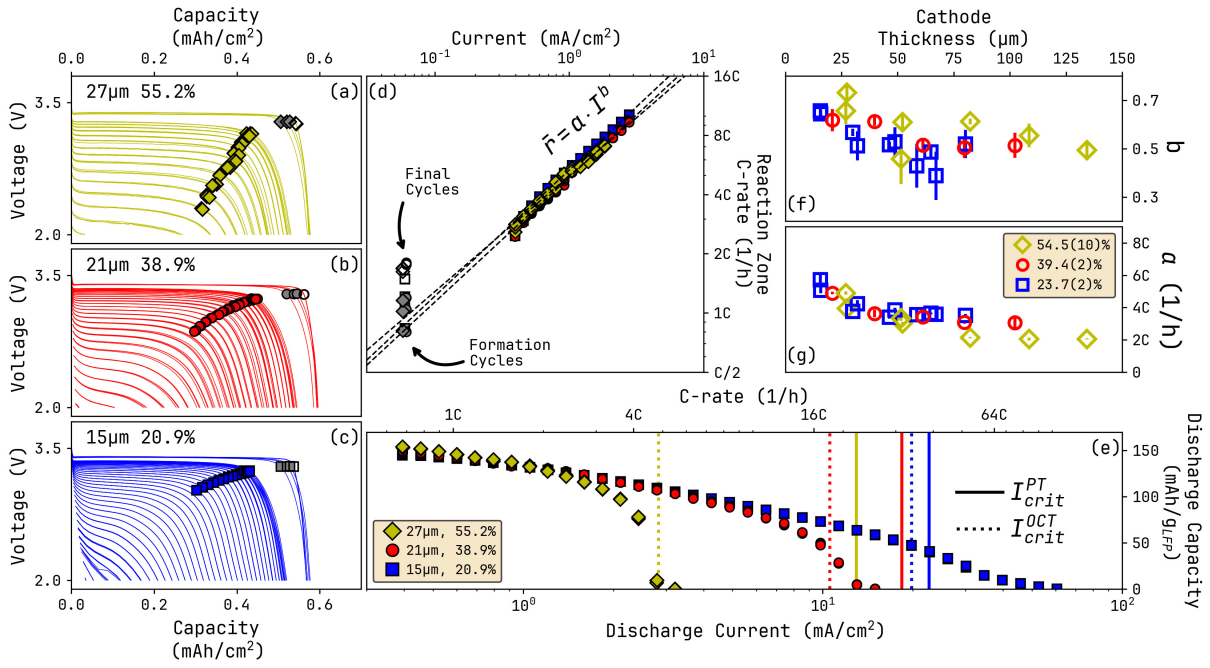

Figure 4: Analysis of the phase-transformation rate-limiting mechanism. (a-c) show galvanostatic discharge curves of three LFP|Li-metal $0.58\,\mathrm{mAh\,cm^{-2}}$ coin cells with cathodes of different porosities, discharged across a series of currents. The markers mark the moment when the cell voltage starts to diverge. The markers in (d) represent the average reaction zone C-rate calculated using equation 8, plotted against discharge current. The dashed lines are power-law fits of the reaction zone C-rates. The markers in (e) represent the discharge capacities of the three cells plotted against discharge current. The top axis shows the C-rate and is calculated with $R = I\overline{Q_A}^{-1}$, where $\overline{Q_A}$ is the average nominal areal capacity of the three cells. The solid vertical lines represent the PT critical currents calculated by extrapolating the fits in (d) to the current where the cell C-rate matches the average reaction zone C-rate. The dotted vertical lines represents the OCT critical currents. Figures (f-g) show the coefficient and the exponent of the power-law fits for all 86 coin cells. Each marker represents the average slope of 3-4 identical coin cells and the error bars represent their standard deviation.

6. Rate-Limits at High Currents

At high currents, the geometry of the cathode becomes consequential. In many analytic studies of ionic liquid-diffusion limited discharges, the critical current is found to be inversely proportional to the cathode thickness[20]. This conclusion is viewed as a hallmark of ILD limited discharges and is often used to identify the mechanism[35,36,52]. As we shall see in the next section, this is true only for thick cathode, and the ILD critical current is reduced in medium-to-thin cathodes. A broader analysis was done in 2020 where the concentration profile across the separator and anode[21]. Here, we use the methods in their analysis to find expressions for the critical current in moving zone reactions (MZR) and uniform reactions (UR). We then compare the critical current from this model with the sharp capacity drop current in our ILD limited coin cells.

6.1. Ionic Liquid-Diffusion Rate-Limit

In this section, we derive simple expressions for the concentration profiles in moving zone reactions and in uniform reactions. In both cases we use the mass conservation, stating that the change in concentration ($\partial c/\partial t$) at any time and location is the amount that diffuses into the location ($\nabla(D\nabla c)$) minus the amount that is intercalating into the cathode active material (i_r).

$$\frac{\partial c}{\partial t} = \nabla(D\nabla c) - i_r \tag{10}$$

where $\partial c/\partial t$, D, and i_r are the change in local electrolyte concentration, diffusion coefficient, and local reaction rate. We further assume that the system reaches a quasi steady-state where the concentration gradient changes only slowly ($\partial c/\partial t \approx 0$) and that the diffusion coefficient is independent of electrolyte concentration ($\nabla(D\nabla c) = D\nabla^2 c$). We also use the charge neutrality condition that the total amount lithium dissolved in the electrolyte does not change.

$$c_0(L_{an}\varepsilon_{an} + L_{sep}\varepsilon_{sep} + L_{cat}\varepsilon_{cat}) = \int_{x_{ac}}^{x_{cc}} c(x)\varepsilon(x)\mathrm{d}x \tag{11}$$

where c_0 is the initial concentration, and $L_{an/sep/cat}$ and $\varepsilon_{an/sep/cat}$ are the thickness and porosity of the anode, separator, and cathode. We now set the boundary conditions that define the discharge dynamics. We begin with the moving zone reaction[21,53]. In an idealized moving zone reaction, the cell current is confined to an infinitesimally thin zone in the cathode. This means that $i_r = 0$ and $D\nabla^2 c = 0$ (from Equation 10) elsewhere, resulting in a set of linear concentration gradients. The slope is J/D_{cat}, where J is the lithium-ion flux and D is the diffusion coefficient through the cathode. The ion flux is proportional to the discharge current with Faraday's law ($J = I/nF$). The resulting concentration gradient is shown below.

$$c_{cat}^{MZR}(x) = \begin{cases} c_r + \dfrac{J}{D_{cat}}(x_r - x) & 0 \le x < x_r \quad \text{(Surface Region)} \\ c_r & x_r \le x \le x_{cc} \quad \text{(Deep Region)} \end{cases} \tag{12}$$

where c_r is the concentration at the reaction zone and beyond and x_r is the distance from the cathode surface to the reaction zone. We now turn to the uniform reaction, where the reaction rate is distributed uniformly across the cathode with $i_r > 0$. Equation 10 then dictates that the curvature of the concentration profile is $\nabla^2 c = i_r/D$. In addition, the flux into the cathode from the separator and the absence of flux into the current collector determines the slopes at those locations, with $\nabla c(0) = J/D_{cat}$ and $\nabla c(L_{cat}) = 0$.

$$c_{cat}^{UR}(x) = c_{cc} + \frac{J}{D_{cat}L_{cat}}\frac{(x - x_{cc})^2}{2} \quad x_{sc} \leq x < x_{cc} \tag{13}$$

where the subscripts cc and sc refer to the cathode current collector and the separator-cathode interface, respectively. There is no reaction in the separator, and its profile is similar to that in the MZR case.

$$c_{sep}(x) = c_{sc} + \frac{J}{D_{sep}}(x_r - x) \quad x_{as} \leq x < x_{sc} \tag{14}$$

The profiles in the anode are similar, except that $i_r < 0$. Below are the concentration profiles in the anode.

$$c_{an}^{MZR}(x) = \begin{cases} c_{as} - \dfrac{J}{D_{an}}(x - x_{as}) & x_{as} - x_r^{an} \leq x < x_{as} \quad \text{(Surface Region)} \\ c_{as} + \dfrac{J}{D_{an}}x_r^{an} & x_{ac} \leq x \leq x_{as} - x_r^{an} \quad \text{(Deep Region)} \end{cases} \tag{15}$$

where the subscript as refers to the anode-separator interface and x_r^{an} is the distance to the reaction zone in the anode. Next, the uniform reaction.

$$c_{an}^{UR}(x) = c_{as} - \frac{JL_{an}}{2D_{an}}\left(1 - \frac{(x - x_{ac})^2}{L_{an}^2}\right) \tag{16}$$

where the subscript ac refers to the anode current collector. We can now construct concentration profiles across the whole cell. Once these have been constructed, we can use Equation 11 to normalize the concentrations and find I_{crit}^{ILD}, the current at which the electrolyte is depleted by the end of discharge ($c_{cc} = 0$ when $x_r = L_{cat}$). This yields the critical current

$$I_{crit}^{ILD} = \frac{I_d}{\Lambda^{cat|an}} \tag{17}$$

where $\Lambda^{cat|an}$ represents the average concentration in the cathode relative the initial and I_d is the diffusion limited current, given by

$$I_d = \frac{2nFD_{cat}c_0}{L_{cat}} \tag{18}$$

We calculate $\Lambda^{an|cat}$ for all combinations of discharge modes in the anode and cathode. These are listed below.

$$\Lambda^{MZR|MZR} = \nu_{cat} + \nu_{sep}(2 + \kappa_{sep}) + \nu_{an}\left(2 + \kappa_{sep} + \kappa_{an}\left(\frac{3}{2} - \frac{1}{q}\right)\right) \tag{19}$$

$$\Lambda^{MZR|UR} = \frac{\nu_{cat}}{3} + \nu_{sep}(1 + \kappa_{sep}) + \nu_{an}\left(1 + \kappa_{sep} + \kappa_{an}\left(\frac{3}{2} - \frac{1}{q}\right)\right) \tag{20}$$

$$\Lambda^{UR|MZR} = \nu_{cat} + \nu_{sep}(2 + \kappa_{sep}) + \nu_{an}\left(2 + \kappa_{sep} + \frac{2}{3}\kappa_{an}\right) \tag{21}$$

$$\Lambda^{UR|UR} = \frac{\nu_{cat}}{3} + \nu_{sep}(1 + \kappa_{sep}) + \nu_{an}\left(1 + \kappa_{sep} + \frac{2}{3}\kappa_{an}\right) \tag{22}$$

$\nu_{cat/sep/an}$ and $\kappa_{sep/an}$ are the relative pore volumes and the concentration drop in the separator and anode relative that in the cathode. q is the NP-ratio, the ratio between capacity in the anode and the cathode.

$$\nu_i = \frac{L_i\varepsilon_i}{L_{cat}\varepsilon_{cat} + L_{sep}\varepsilon_{sep} + L_{an}\varepsilon_{an}} \quad \kappa_i = \frac{L_i/D_i}{L_{cat}/D_{cat}} \tag{23}$$

All six cells are shown in Figures 5a-f, with cathodes to the right and anodes to the left. The yellow electrodes have a UR type concentration profile and the red electrodes have an MZR type profile. The profiles are shown with a shaded dark blue region. We see that the to lithium metal anode cells have much larger cathodes than the others. This is because much more of the electrolyte is retained within the cathode. In the cells with porous anodes (c-f), the concentration profile shifts to the left, limiting the penetration depth into the cathode. In Figure 5g, the critical current is plotted against cathode thickness for each of combination of electrodes. The lithium metal anode cells have a much larger critical current than those with porous anodes. This difference has been noted in previous analyses[1,21]. The dotted lines show the critical current at the no-separator limit in the metal anode cells, following the inverse-power-law in Equation 18. We see that the separator has a great impact on the critical current of the UR cathode, but less so on that of the MZR cathode. The porous anode cells are mostly independent of separator. This is because the separator is a much smaller portion of the total pore volume. However, the impact of the separator is diminished in thick cathodes, in which the ILD is the most relevant.

Both UR and MZR concentration profiles are highly idealized, and in reality the discharge dynamic will exhibit a mixture of both. Cathodes with a narrow reaction potential with respect, such as LFP, exhibit more of a MZR character while those with a broad and concentration-dependent reaction potential, like NMC, exhibit a character closer to UR. As discussed in Section 5.2, the reaction zone in LFP grows with current, approaching the UR discharge at high currents. Graphite has a piece-wise combination, where the potential is highly concentration-dependent at low concentrations and become flat towards the end[21]. The analysis here shows the impact these differences may have on the ILD critical current.

Many of the LFP and NMC cells exhibited the ILD rate-limiting mechanism. As discussed in previous sections, these active materials exhibit different discharge dynamics

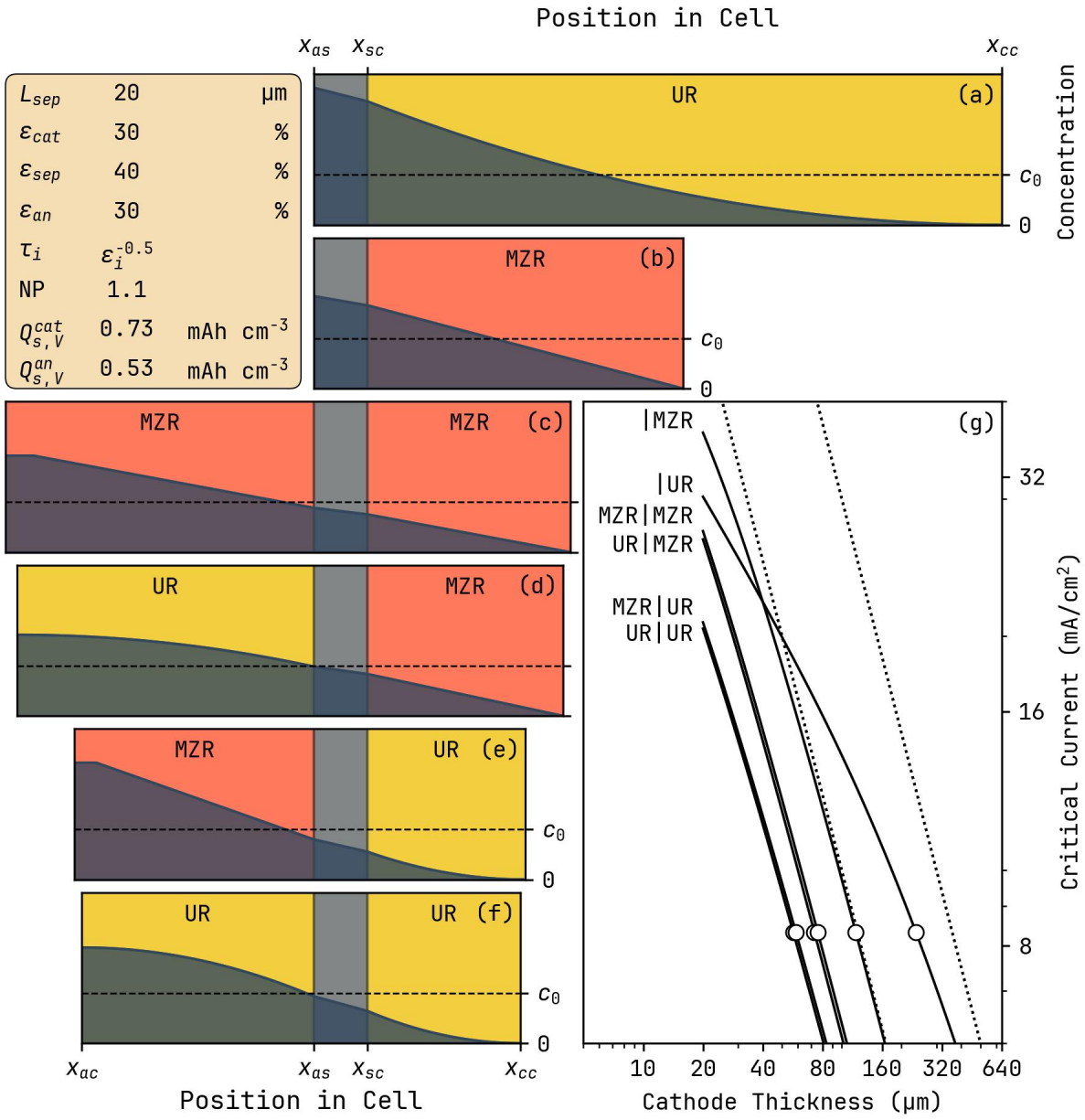

Figure 5: Critical Currents with different discharge modes. (a-f) shows the concentration profiles of six cells with different types of anodes and cathodes, discharging at the same critical current, such that they reach electrolyte depletion. Anodes are shown to the left and the cathodes to the right. The yellow electrodes have a UR type concentration profile and the red electrodes have an MZR type profile. The six panels share scale and line up on the gray separator, sorted by cathode thickness. The cells in (a-b) have Li-metal anodes. The concentration profiles are shown with a shaded dark blue region. The details of the model are shown in the box in northwest corner. The solid lines in (g) represent the critical currents of the six types of cells as a function of cathode thickness. The white circles mark the cells in (a-f). The dotted lines mark the no-separator critical currents for the two cells with metal anodes.

that are expected to show up in the ILD limit. Here, we plot the measured ILD critical current against cathode thickness, compare the trends with our expectations from the previous section, and calculate empirical proportionality constants.

Figure 6a shows the capacity-drop current of all ILD-limited LFP cells (red diamonds) and ILD-limited NMC cells (blue markers) from work published in Ref.[1], plotted as a function of cathode thickness. Each marker represents the geometric mean critical current among 3–4 coin cells, with error bars indicating the logarithmic standard deviation. We find that the critical currents of the LFP cathodes match those of NMC cathodes with similar porosity. This contrasts with the modeling in the previous predicting that a moving reaction zone would result in a lower critical current than that of a uniform reaction. The cathodes studied here differ morphologically, including in tortuosity, which affects ionic liquid diffusion and is not controlled for in this work. This may explain the higher critical current in our LFP cathodes. On the other hand, the NMC cathodes seem to deviate more from the inverse-power-law than the LFP cathodes do. This is a feature of UR|metal cells.

The dotted lines represent log–log fits of the form $I_{crit}^{ILD} = CL_{cat}^{-1}$, grouped by porosity and cathode material. For the NMC cells, only the three thickest cathode groups at each porosity are included to minimize separator-volume effects present in thinner cathodes. Table 5 shows the geometric mean values of the measured proportionality constants $L_{cat}I_{crit}^{ILD}$ and $\varepsilon_{cat}^{-1}L_{cat}I_{crit}^{ILD}$ for each group of cathodes. These can be used to find the optimal cathode thickness for a given application. For example, the critical currents of the dense LFP cathodes can be described by

$$L_{opt} \approx \frac{704\ \mu\mathrm{m\,mA\,cm^{-2}}}{I_{crit}^{ILD}} \approx \frac{\varepsilon_{cat}}{I_{crit}^{ILD}} \cdot 2878\ \mu\mathrm{m\,mA\,cm^{-2}}. \tag{24}$$

It is often more useful to express this relationship in terms of C-rate, R, and areal capacity, Q_A. Using $I = RQ_A$ and $L_{cat} = Q_A(1-\varepsilon_{cat})^{-1}Q_{V,s}^{-1}$, and taking the dense LFP cathodes to have a geometric mean volumetric capacity of $Q_{V,s} \approx 461\,\mathrm{mAh\,cm^{-3}}$, we obtain the following expression for the ILD-limited critical C-rate:

$$R_{crit}^{ILD} \approx \frac{15\ \mathrm{h(mAh/cm^2)^2}}{Q_A^2} \approx \frac{\varepsilon_{cat}(1-\varepsilon_{cat})}{Q_A^2} 83\ \mathrm{h(mAh/cm^2)^2}. \tag{25}$$

The geometric mean proportionality constants $Q_A^2 R_{crit}^{ILD}$ for each cathode set are listed in Table 5. Extrapolating these fits to a C/3 discharge rate (white markers) provides an estimate of the maximum practical cathode thickness. We find that the densest LFP cathodes could reach thicknesses of approximately 248 µm, with similar values obtained for NMC. However, the higher specific capacity of NMC results in larger attainable cell capacities, as shown in Figure 6b, where the critical C-rate is plotted against nominal capacity. The optimal cathode thickness for 1 C discharge and the corresponding areal capacity are summarized in Table 5 in Appendix 13.

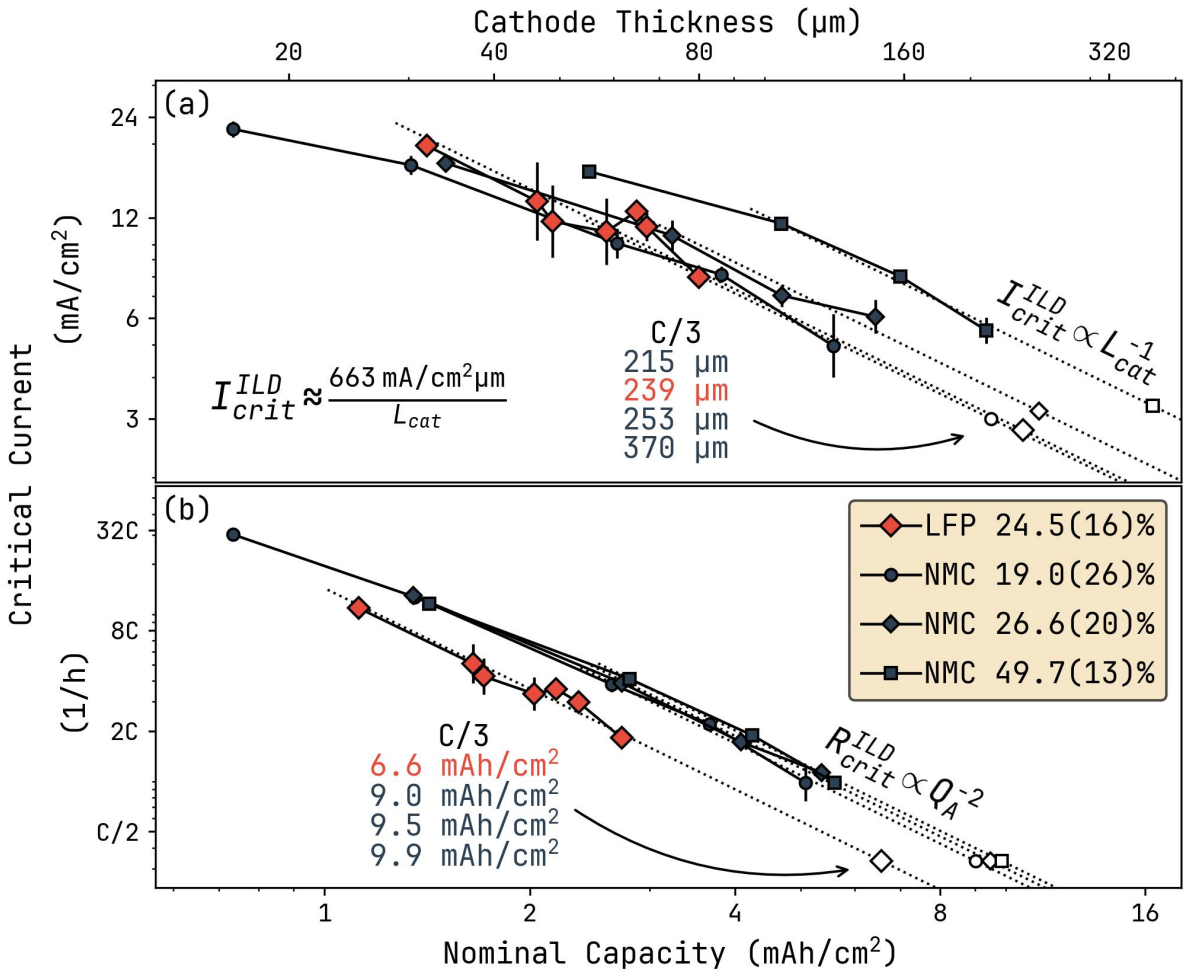

Figure 6: Analysis of ionic-liquid diffusion (ILD) critical currents on log–log axes. (a) ILD critical current density I^{ILD}_{crit} (mA cm^{-2}) as a function of cathode thickness L_{cat} (µm), and (b) critical C-rate R^{ILD}_{crit} (h^{-1}) as a function of nominal areal capacity Q_A (mAh cm^{-2}). LFP|Li-metal cells are shown as red diamonds, and NMC|Li-metal cells as blue circles, diamonds, and squares. The legend lists the arithmetic mean cathode porosity, with parenthetical values indicating the arithmetic standard deviation, consistent with porosity labeling throughout the manuscript. Dotted lines in (a) and (b) correspond to the scaling relations $I^{ILD}_{crit} \propto L_{cat}^{-1}$ and $R^{ILD}_{crit} \propto Q_A^{-2}$, respectively. Fits to the NMC data are restricted to the three thickest cathode sets. White markers indicate the cathode thickness and nominal capacity extrapolated to a critical C-rate of C/3. NMC data are taken from Ref.[1].

6.2. Ohmic/Charge-Transfer Rate-Limit

In the next two sections, we look at the OCT voltage in the experimental data. We use a section of the discharge curve at low currents to estimate ΔV_{OCT} and its behavior with respect to discharge current. We then extrapolate the trend to find the OCT critical current, I^{OCT}_{crit}, beyond which the polarization exceeds the margin voltage, ΔV_{margin}, result-

ing in severe underutilization. In the first section, we focus on LFP, for which most cells were OCT-limited. We show that, although the OCT voltage is proportional to discharge voltage, the Ohmic potential does not seem to be a major contributor, as $d\Delta V_{OCT}/dI$ is mostly independent of cathode thickness. The next section focuses on our NMC cells, most of which were ILD-limited. We use these cells to investigate the impact of the margin voltage, by analyzing the rate performance evaluated at different lower threshold voltages. We show that the critical currents enters the OCT regime at threshold voltages at and above 2.5 V. This is significant, as much of the literature use these threshold voltages, leaving the cause of the sharp capacity drop ambiguous.

6.2.1. Ohmic/Charge-Transfer Rate-Limit in LFP Cathodes

At low currents, the continuously decreasing applied voltage corresponds to the increasing electrochemical potentials as the distance from the current collectors to the reaction zone changes. Figure 7 shows the analysis of this region of the discharge curves. Figures 7a-c show discharge curves of three LFP|Li-metal cells with similar cathode thickness, but with different porosities. We fit a line to a narrow section of the plateau regions of the discharge curves. The fit is limited to a narrow section to avoid the influence from the slowly evolving electrolyte concentration and electrolyte resistivity. The section is placed at a quarter of the nominal capacity and spans a range of 0.1 mAh cm^{-2}, marked with black points. This aims to ensure that the fit spans a specific reaction zone location within the cathode. The analysis is limited to those cycles for which this range lies within the plateau region and contains at least 4 data points.

The intercepts of the linear fits are plotted against discharge current in Figure 7d. The drop in the intercept with respect to current corresponds to the ionic resistance of the electrolyte through the separator and a quarter of the cathode, the electronic resistance through the remaining three quarters of the cathode, and overpotentials at the anode and reaction zone. Although this voltage drop is expected to exhibit both a linear and logarithmic term, the data shows a predominant linear character. Therefore, the voltage drop is fitted linearly, shown with dashed lines in Figure 7d. Extrapolating the voltage drop to the threshold voltage yields the Ohmic/charge-transfer critical current, I_{crit}^{OCT}, shown below.

$$I_{crit}^{OCT} = \frac{U - V_{thresh}}{\mathrm{d}V/\mathrm{d}I} \tag{26}$$

Where V_{thresh} is the threshold voltage (here 2.0 V) and U and $\mathrm{d}V/\mathrm{d}I$ are fitting parameters from the fit of the voltage drop. The markers in Figure 7e represent the discharge capacity of the three cells plotted against specific discharge current and the three vertical lines mark their extrapolated I_{crit}^{OCT}. The extrapolated critical currents of the two more porous cathodes match the sharp capacity drop very well. Inspecting the discharge curves, we see that their sharp capacity drop corresponds to discharges reaching the threshold voltage before the end of discharge; a hallmark of OCT limited discharges. In contrast, most dense cathode exhibits a sharp capacity drop at a current much lower than the OCT critical

current. Its discharge curves show that the capacity drop corresponds to the voltage diverging before reaching the end of discharge; a hallmark of ILD limited discharges.

Figure 7f shows the voltage drop ($\mathrm{d}V/\mathrm{d}I$) of 86 cells across with cathodes across a range of thicknesses and porosities. Each marker in 7f represents the average $\mathrm{d}V/\mathrm{d}I$ among 3–4 identical coin cells and the error bar represents their standard deviation. $\mathrm{d}V/\mathrm{d}I$ increases with increasing porosity but is mostly independent of cathode thickness.

The linear voltage drop with respect to current and its reduction with increasing density is consistent with a large Ohmic contribution. However, its independence on cathode thickness runs counter to this conclusion. The larger cathodes have a smaller voltage drop than what would be expected in a predominant Ohmic contribution. As discussed in Section 5.2, this may be explained by the cell current being delivered by a larger number of LFP particles in thicker cathodes. This would result in a smaller overpotential and larger surface area, thus reducing the voltage drop in larger cathodes.

6.2.2. Interplay of Rate-Limiting Mechanisms in LFP

As discussed in the previous sections, the various rate-limiting mechanisms depend on cathode thickness and porosity in different ways. In this section, we pull together the analysis of the PT, OCT, and ILD in LFP cathodes. Figure 8 displays the discharge current at the sharp capacity drops (I_{drop}), represented by circles colored according to the rate-limiting mechanism (yellow for OCT, red for PT, and teal for ILD). Additionally, the OCT and PT critical currents, denoted as yellow squares and red diamonds respectively, are calculated using equations 26 and 9, plotted against the cathode thickness. Figures 8a, b, and c present data from cathodes with porosities of 54.5(10) %, 39.4(2) %, and 23.6(2) %, respectively.

Our analysis reveals that the capacity drop in the two more porous sets of cathodes (Figures 8a and b) is exclusively governed by the OCT rate-limiting mechanism, with the observed discharge current, I_{drop}, aligning closely with the OCT critical current I_{crit}^{OCT} (yellow squares). Notably, I_{crit}^{OCT} remains predominantly independent of cathode thickness while exhibiting a decrease with porosity. This observation aligns with results reported for NMC cathodes in Ref.[1], suggesting that Ohmic potentials across the electrolyte and the conductive matrix of the cathode are not significant contributors to the overall voltage drop, as these display a pronounced thickness dependence[53]. Alternatively, the thicker cathodes may mitigate Ohmic potential effects by distributing the current across a greater number of particles, thus reducing surface overpotentials, as discussed in Section 5.2

When the porosity is decreased further, to 23.6(2) % (Figure 8c), I_{crit}^{OCT} increases from $\sim$10 mA cm^{-2} to $\sim$20 mA cm^{-2}, while I_{drop} develops an inverse relationship to cathode thickness, with I_{drop} remaining mostly unchanged among thicker cathodes. This is attributed to the dominance of the ILD mechanism (teal circles) in the capacity drop, as opposed to OCT. The thinner cathodes exhibit the PT mechanism (red circles), with I_{drop} aligning with the predicted PT critical current I_{crit}^{PT} (red diamonds). In most other cathodes, I_{crit}^{PT} is significantly higher than I_{drop}. Despite the PT mechanism being primarily relevant for the densest, thinnest cathodes, the relationship between I_{crit}^{PT} and nominal capacity,

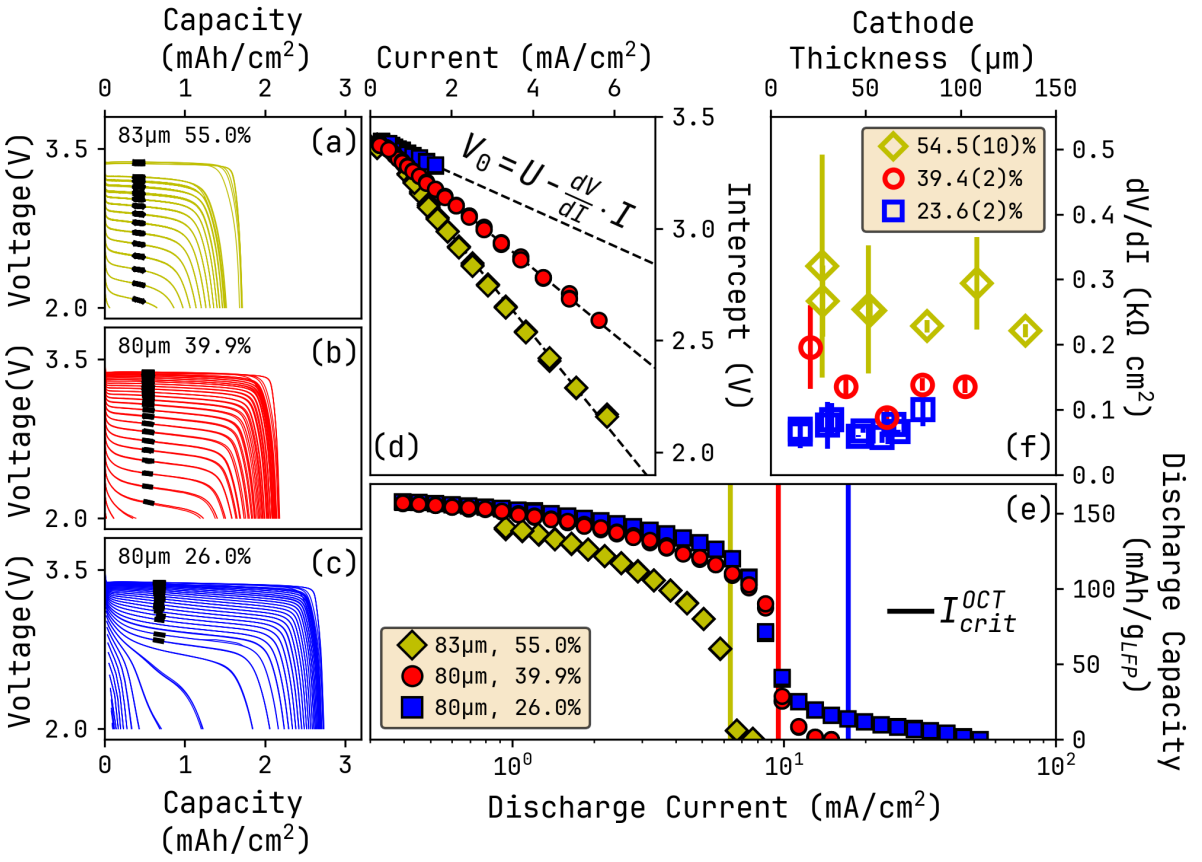

Figure 7: Analysis of the Ohmic/charge-transfer rate-limiting mechanism. (a-c) show galvanostatic discharge curves of three LFP|Li-metal coin cells with 80 µm thick cathodes of different porosities, discharged across a series of currents. The black markers indicate the region that is used for the linear fits. The markers in (d) represent the intercepts of the linear fits of the discharge curves plotted against discharge current. The dashed lines are linear fits of the intercepts. The markers in (e) represent the discharge capacities of the three cells plotted against discharge current. The vertical lines represent the OCT critical currents calculated by extrapolating the fits in (d) to the threshold voltage. Figure (f) shows the slopes (dV/dI) of the linear fits for all 86 coin cells. Each marker represents the average slope of 3–4 identical coin cells and the error bars represent their standard deviation.

described in equation 9, provides important insights. Given that the phase-transformation limit is characterized by the full utilization of the cathode, it makes sense that it increases with loading Q_A. This increase is, however, moderated by the apparently lower average reaction zone C-rate in thicker cathodes, causing the full utilization of the cathode at lower cell currents. Absent these effects, one would anticipate that I^{PT}_{crit} would correlate approximately with Q_A^2 ($b \approx 0.5$ and $da/dQ_A = 0$ in equation 9). Instead, I^{PT}_{crit} is proportional to less than Q_A ($Q_A^{0.22}$, $Q_A^{0.94}$, $Q_A^{0.64}$ for porous, mid, and dense cathodes, respectively).

Overall, we observe three competing rate-limiting mechanisms that evolve with cathode thickness and porosity that limit the discharge current. Exceeding the critical currents associated with any of these mechanisms severely limits the discharge capacity. Notably, within these cells, the primary limitation arises from the OCT mechanism. It is only by calendering the cathodes to very low porosity that the OCT limit is elevated sufficiently while the ILD limit is reduced, thereby transitioning to ILD-limited behavior. Furthermore, the cells in this study were discharged to a notably low threshold voltage of 2.0 V, which serves to further elevate the OCT limit (see equation 26) [1]. In the next section, we use NMC to show the impact of the choice of the lower threshold on the rate-limiting mechanism.

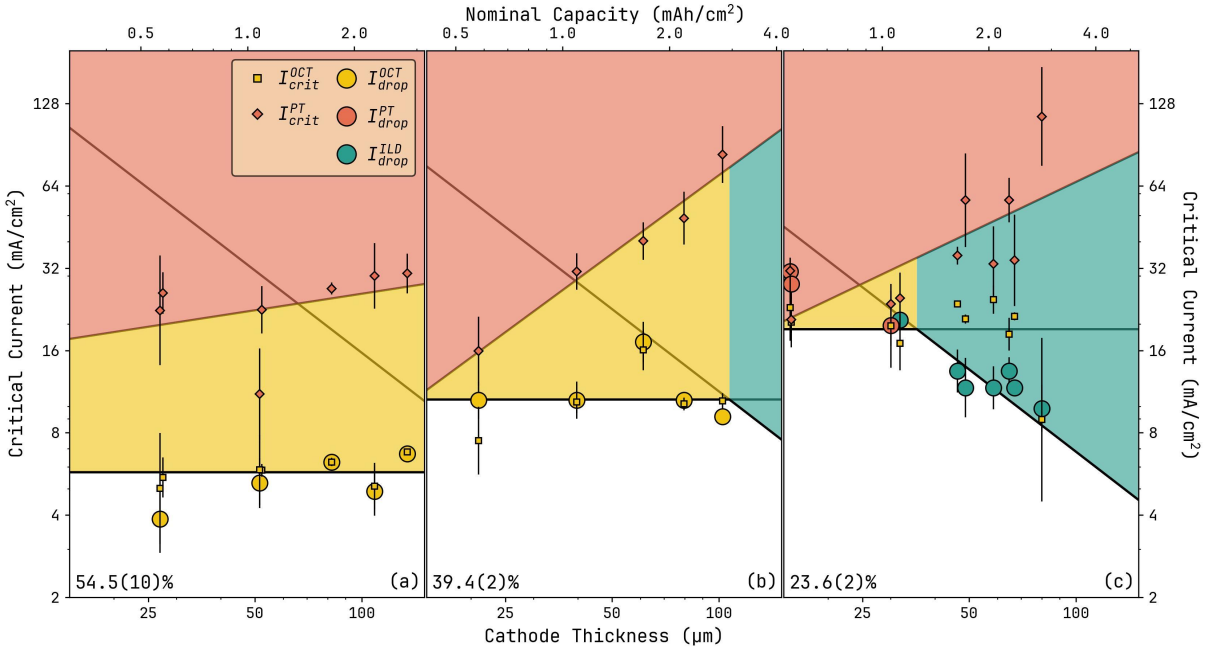

Figure 8: Critical currents and capacity drop currents plotted against cathode thickness (log-log axes) for all 86 LFP|Li-metal cells. Each marker represents the geometric average of 3–4 identical cells, and the error bars their geometric standard deviation. Subplots (a), (b), and (c) show data from cells with similar porosities of 54.5(10) %, 39.4(2) %, and 23.6(2) %, respectively, plotted against cathode thickness (bottom axes). The top axes shows the nominal capacity of the cells and are calculated with $Q_A = \overline{Q_V} L_{cat}$, where $\overline{Q_V}$ is the average nominal volumetric capacity of the cells in the subplot. The discharge currents at the capacity drop, I_{drop}, are marked with circles. Their colors represent the rate-limiting mechanisms OCT (yellow), PT (red), and ILD (teal). Yellow squares and red diamonds mark the calculated OCT and PT critical currents, I^{OCT}_{crit} and I^{PT}_{crit}, respectively. The horizontal line at the bottom of the yellow region is the geometric mean of I^{OCT}_{crit}. The line at the bottom of the red region is the log-log fit of $I^{PT}_{crit} = C_1 \cdot L^{C_2}_{cat}$. The line at the bottom of the teal region is the log-log fit of $I^{ILD}_{drop} = C \cdot \varepsilon_{cat} L^{-1}_{cat}$ (calculated from the ILD limited data in (c)).

6.2.3. The Impact of the Lower Threshold Voltage on the Critical Current

The OCT limit is the current at which the polarization exceeds the margin voltage. The margin voltage is the difference between the equilibrium voltage at full filling and the threshold voltage. This means that the operational parameter of the threshold voltage has a significant impact on the rate performance of the cell. Figure 9 illustrates this effect. The capacity drop mechanism can be interpreted by inspecting the evolution of galvanostatic discharge curves over a series of discharge currents, shown for two NMC|Li-metal cells with cathodes of different thicknesses in Figures 9a and b. In Figure 9b, showing the discharge curves of a thick cathode (213 µm), each discharge ends with the voltage diverging towards the threshold voltage. The high-current discharge curves of the thin cathode (29 µm, Figure 9a), on the other hand, reach the threshold voltage before diverging. This suggests that the thin cathode is OCT-limited. We use Equation 26 to investigate further. Simulations of porous electrode theory suggest that cathodes with solid-solution active materials, such as NMC, quickly form quasi-steady-state distributions that persist for most of the discharge [21]. As such, the initial voltage drop measured as soon as these distributions have formed will be used to estimate ΔV_{OCT}. This is done by fitting the early portion of the discharge curve (here chosen as $q < 0.3Q_M$) with Equation 27.

$$V_{cell} \approx V_0 - \Delta V_{OCT} + kq + a\exp\left(-\frac{q^c}{b}\right) \tag{27}$$

where q is the discharged capacity and k, a, b, and c are four fitting parameters. This fitting is shown for a selection of discharge curves in the inset of Figure 9a and the resulting ΔV_{OCT} from both cathodes are shown with yellow diamonds and teal circles in Figure 9c, plotted against discharge current. In order to estimate the OCT-limit, ΔV_{OCT} is fitted against discharge current using Equation 28 [54].

$$\Delta V_{OCT} \approx IR_{Ohm} - \frac{RT}{\alpha F}\ln\left(\frac{I}{i_0}\right) \tag{28}$$

where I is the discharge current, R_{Ohm} is the cell resistance, and i_0 is the cell level exchange current density. Equation 28 takes into account the contributions from the Ohmic resistance across the cell and the overpotentials at the anode and cathode interfaces. However, due to SEI growth and the evolution of the morphology of the Li-metal anode, in particular when paired with high loading cathodes, R_{Ohm} and i_0 are expected to evolve somewhat throughout the experiment. This limits the use of the fit to that of a rough estimate of the current-dependence of ΔV_{OCT}. Equation 28 is shown fitted to data in Figure 9c with teal and yellow dashed lines. The fit marks the boundary right of which (shaded grey) the discharge capacity will be significantly limited by Ohmic/charge-transfer losses. Extrapolating the fit to the margin voltages of 1.65 V and 1.56 V yields the OCT-limits 25.8 mA cm^{-2} and 29.6 mA cm^{-2}, respectively, marked with horizontal and vertical dotted lines in Figures 9c and d. Figure 9d shows the discharge capacities of the two cells plotted against discharge current density in units of mA cm^{-2}. The higher discharge capacity in the thicker (higher loading) cathode reflects its lower C-rate when discharged at the same

current density as the thinner (lower loading) cathode. The critical currents are marked by white markers at their respective capacity drop. In the case of the thin cathode, the capacity drops sharply when the current reaches the OCT-limit. In contrast, the thick cathode experiences a sharp capacity drop at a much lower current. This suggests that the capacity drop in the thin cathode is mainly caused by the OCT-limit, while it is caused by some other effect in the thick electrode. Given its larger size and the diverging voltage at the end of the discharges, the sharp capacity drop in the thick cathode is likely caused by ILD-limits.

Equation 26 shows that the OCT-limit is strongly dependent on the choice of lower threshold voltage, V_t. In order to illustrate this effect, the discharge capacity and critical current are evaluated at different threshold voltages up to 3.4 V, marked with a red solid line in Figures 9a, b, c, and d. That is to say, the discharge curves are cut off at a higher threshold voltage and the discharged capacities at this voltage are used as discharge capacities for the purpose of calculating the critical current. The horizontal red dotted line in Figure 9b marks the lower threshold voltage of 3.0 V and the vertical red solid line to the right of the discharge curves illustrate the resulting margin voltage, ΔV_{margin}. The discharge capacities at this lower threshold voltage are shown in Figure 9d with open markers. The discharge capacities are lower at this lower threshold voltage and the critical current is shifted to lower currents, marked by red markers. Note that the critical current shifts much further in the thin cathode than in the thick cathode, such that they have very similar critical currents at the 3.0 V threshold voltage. This effect is better illustrated in Figure 9c, where the critical currents are shown as a function of ΔV_{margin}. Starting from the white markers at $V_t = 2.0$ V, as the lower threshold voltage increases towards 3.0 V, the margin voltage decreases and the critical currents follow the red lines to the red markers. The critical current in the thin cathode (red/white diamond marker) follow the edge of the OCT-limit. In contrast, the critical current in the thick cathode (red/white circle marker) changes negligibly until it reaches the OCT-limit at around $V_t = 3.0$ V, beyond which it starts decreasing sharply as it follows the edge of the OCT limit. These results show that the critical current is strongly dependent on the lower threshold voltage in thin cathodes, while it is very weakly dependent in thick cathodes at lower threshold voltages below 3.0 V. This implies that the discharge rate in thin cathodes are predominantly limited by the OCT limit, rather than ILD limits. Furthermore, it shows that the critical current becomes increasingly independent of cathode thickness as the lower threshold voltage is raised. This is significant as NMC cells are often discharged to a lower threshold voltage of 3.0 V in rate performance experiments, making the rate-limiting mechanisms ambiguous without further analysis[32,36,55].

The analysis in Figure 9 showed that both the critical current and the rate-limiting mechanism depend on both the cathode thickness and the lower threshold voltage. We explore this interplay further by measuring the critical current and analyzing the rate-limiting mechanisms across a range of cathode thicknesses and porosities. Each marker represents the log-average critical current and thickness of each group of 3–4 NMC|Li-metal coin cells. The first thing to note is that the critical current in the thickest cathodes of all three porosities approximately follow an inverse power-law with respect to thickness. The

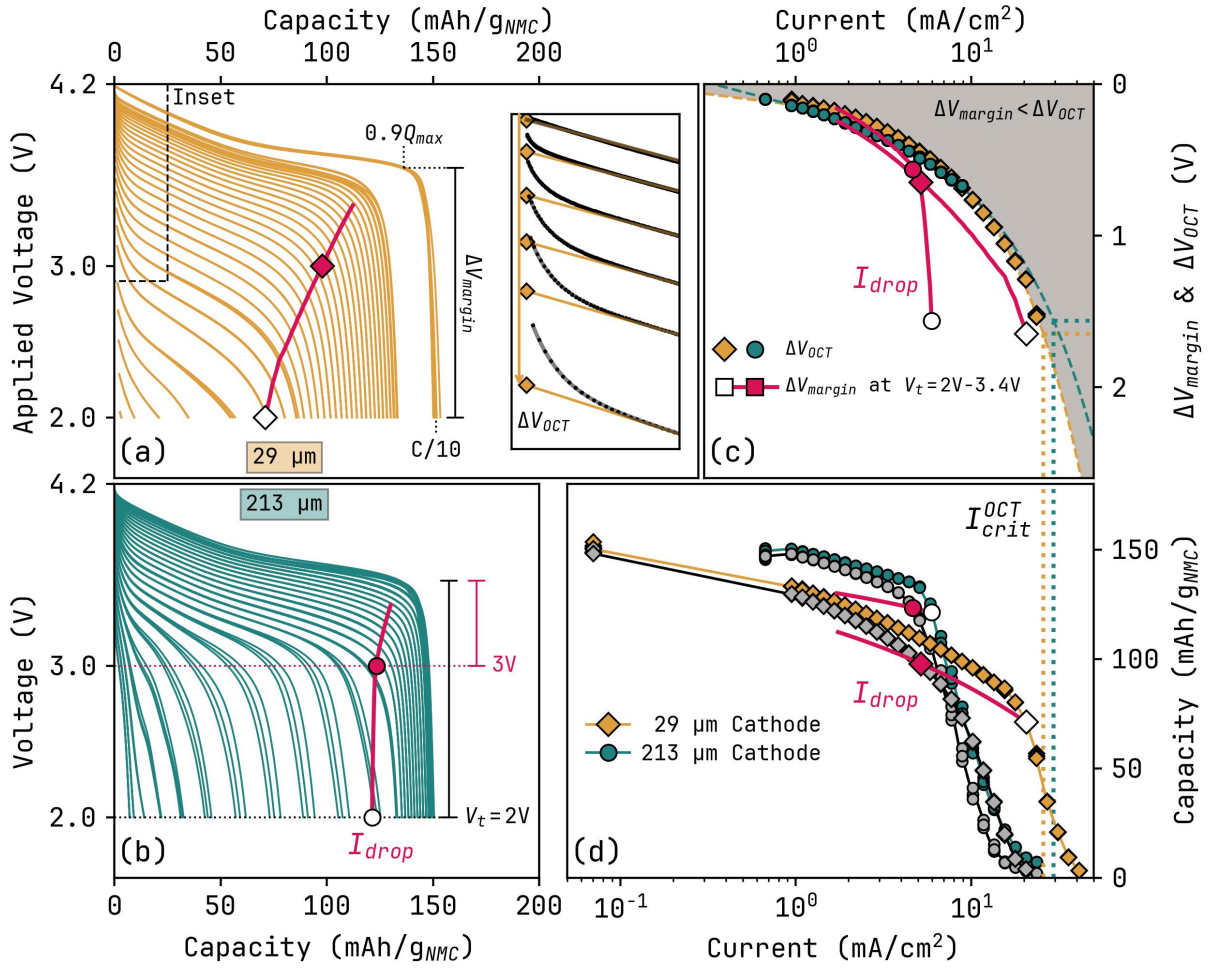

Figure 9: Finding the OCT limit in a thin (29 µm) and a thick (213 µm) NMC cathode across threshold voltages. Figures (a-b) show the discharge curves of the (a) thin and (b) thick cathodes. Figure (c) shows the initial voltage drop of the discharge curves and the critical current calculated at lower threshold voltages from 2.0 V to 3.4 V. Figure (d) shows the rate performance data at lower threshold voltages 2.0 V (closed markers) and 3.0 V (gray markers) as well as the critical current (red solid line, white marker, red marker) as the lower threshold voltage is swept from 2.0 V to 3.4 V.

inverse power-law relationship is shown with three dotted lines as a guide for the eye in Figures 10b-d. In addition, the critical current decreases with decreasing porosity. Both these features are expected in ILD-limited cathodes according to Equation 18. Next, we raise the threshold voltage and see how the rate-limiting mechanisms evolve. In Figure 10a, the dotted lines delineate the OCT-limited cathodes (left) from the ILD-limited cathodes (right) at threshold voltages of 2.0 V, 2.5 V, and 3.0 V. At the experimental threshold voltage of 2.0 V, only the thinnest and most porous group of the cathodes exhibits an OCT rate-limit (yellow diamond in Figure 10b). As the lower threshold voltage is raised to

2.5 V and 3.0 V, thicker and more dense cathodes become OCT-limited as well, until only the thickest cathodes are ILD-limited. Simultaneously, the critical current of the OCT-limited cathodes (yellow markers in Figures 10b-d) decreases as the threshold voltage is raised. At a threshold voltage of 3.0 V (Figure 10d), the few cathodes that are ILD-limited (blue markers), are relatively unaffected by the raised threshold from 2.0 V to 3.0 V. The OCT-limited cathodes, on the other hand, reverse their trend with respect to porosity between 2.0 V and 3.0 V, where the most dense cathodes (yellow circles) evolve to have the highest critical currents.

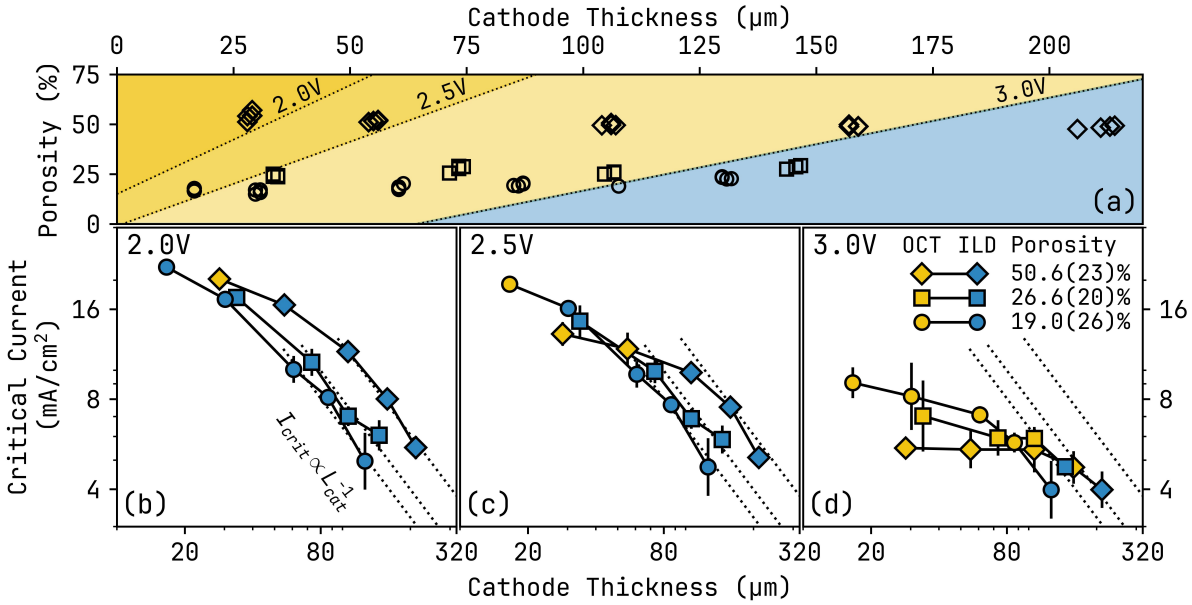

Figure 10: Impact of porosity and threshold voltage. (a) porosity and thickness of all NMC cathodes. Dotted lines delineate OCT-limited cathodes from ILD-limited cathodes at threshold voltages 2.0 V, 2.5 V, and 3.0 V. (b-d) log-log plots of the critical current of three batches of cathodes with different porosities, evaluated at the different threshold voltages. The colors of the markers in (b-d) represent the rate-limiting mechanisms of the cathodes: OCT-limited (yellow) and ILD-limited (blue).

This trend-reversal can be explained by the enhanced conductivity brought by calendering. Figures 11c and d show cross-sectional Scanning Electron Microscopy (SEM) images of two as-received porous cathodes (∼50 % porosity). The large open pores leave the solid phase disconnected, leading to a high contact resistance. This can be seen in Figures 11a and b, showing the Electrochemical Impedance Spectra (EIS) of three cathodes and the corresponding Distribution of Relaxation time (DRT), respectively[56]. At short relaxation times ($\sim 10^{-5} - 10^{-4}$ s), corresponding to contact resistance, we find that the two porous cathodes exhibit a large resistance. Calendering these cathodes presses the network together, as well as improves the contact with the current collector. Figure 11e shows the SEM image of a thick calendered cathode (130 μm, ∼23 % porosity). The solid network in

this cathode is better connected. This is reflected in the DRT spectra in Figure 11b, where the dense cathode exhibits a much smaller contact resistance. The peaks at the longer relaxation times ($\sim 10^{-1} - 10^{1}$ s) correspond to cathode charge transfer and diffusion in solid particles. The thin cathode ($0.7\,\mathrm{mAh\,cm^{-2}}$) exhibits a much greater resistance than the two thick cathodes ($5.6\,\mathrm{mAh\,cm^{-2}}$). This makes sense as these two processes are a function of the total amounts of active material, which the thin cathode has less of. Similar trends in the EIS spectra with respect to thickness have been observed in other studies[18].

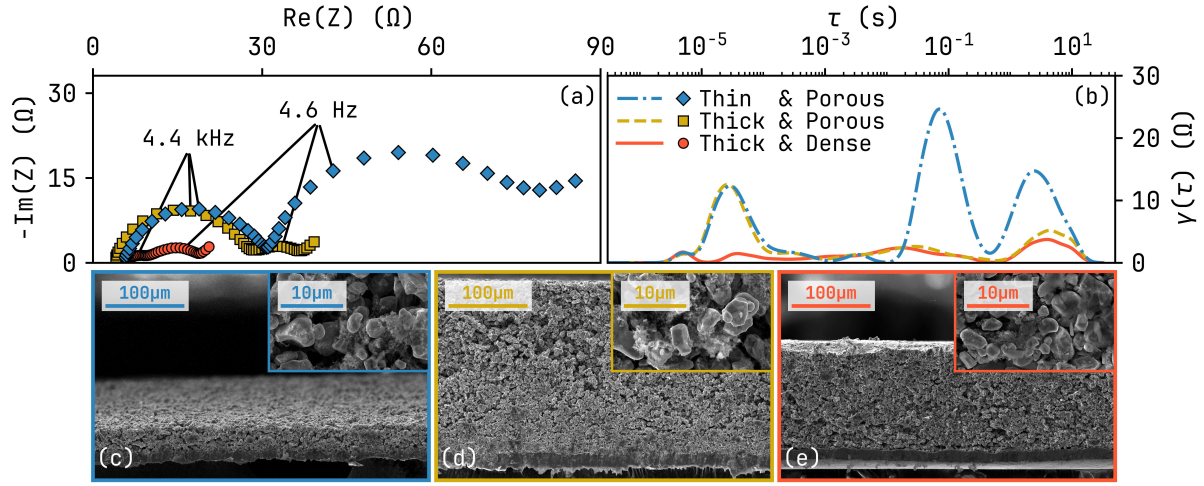

Figure 11: EIS (a) and DRT (b) of three NMC|Li-metal coin cells. SEM images of (c) a Thick & Porous cathode ($5.6\,\mathrm{mAh\,cm^{-2}}$, 216 µm, 47 %), (d) a Thin & Porous cathode ($0.7\,\mathrm{mAh\,cm^{-2}}$, 31 µm, 55 %), and (e) a Thick & Dense cathode ($5.6\,\mathrm{mAh\,cm^{-2}}$, 130 µm, 23 %).

7. Conclusions

In this dissertation, we developed a comprehensive model and framework to characterize and understand the rate-limiting mechanisms in NMC and LFP cathodes for lithium-ion batteries. We support it by creating the largest, highest resolution, and highest quality rate performance data set available in literature[35,36].

We used the voltage drop at the end of LFP discharge curves to show that the actively transforming particles increase both in number and in transformation rate as the cell current is increased. Previous studies have shown that collections of LFP particles prefer activating new particles over increasing the discharge rate of the already-activated particles[15,16,44,57]. These studies focus on small collections of particles, either as thin films or as individual particles. In our study, we use thick LFP cathodes with an abundance of unactivated particles (up until the last moment) and a large cell current, requiring a large number of particles. Our results show that, although an increase in cell current biases towards activating new particles, their average transformation rate also increases by a

similar factor. The discharge curves and rate performance indicate that the thinnest and densest LFP cathodes became phase-transformation limited at 40–60 C, corresponding to a current density of 20–40 mA cm^{-2}, much higher than the asymptotic maximum C-rate of 14.2 C found in chronoamperometry experiments of thin LFP films[16].

The OCT limit is proportional to the margin voltage, which is often chosen as small as possible to stay clear of side reactions at very low applied voltages. This results in all cells being OCT limited until the margin voltage is made large enough to allow for other limits. We illustrate this principle in NMC by evaluating the critical currents and rate limiting mechanisms at different threshold voltages. At a threshold voltage of 3.0 V, only the NMC thickest cathodes were ILD limited, with the rest being OCT limited. The LFP cells primarily suffer from OCT limits at high currents, even with a low threshold voltage of 2.0 V. This limit is pushed to higher currents by calendering and appears independent of cathode thickness. This indicates that the Ohmic resistance of the electrolyte and the solid matrix are not major contributors to the OCT voltage, ΔV_{OCT}. Alternatively, it could be that the Ohmic potential is compensated by the broader distribution of the cell current among the LFP particles.

When thick LFP cathodes are densely calendered to porosities of ∼25 %, the ionic liquid-diffusion becomes limiting instead. In contrast, most NMC cells were primarily ILD limited; with the only exception being the thinnest and most porous cathodes. This limit is inversely proportional to the cathode thickness and further increases to the loading must be compensated with a corresponding reduction in operating current. At normal operating currents of 1 C, we find that the optimum thickness of a dense cathode of either type is in the range of 120–160 µm, corresponding to capacities of around 4 mAh cm^{-2} for LFP and 5.5 mAh cm^{-2} for NMC. The fabrication of a cathode this size often requires new binders or new fabrication techniques to avoid cracking and delamination[26,58,59]. Our model shows that cells with lithium metal anodes have a much higher ILD critical currents than cells with porous anodes. This implies that the optimum cathode thickness of cells with graphite anodes is much smaller. However, it should be noted that lithium metal anodes have much smaller surface areas delivering the cell current. This limits the currents to around 4–10 mAh cm^{-2}, depending on the electrolyte[27–29,60,61]. In addition, lithium metal anodes degrades from plating and stripping large capacities, limiting the cell capacity to below 4 mAh cm^{-2} to maintain cycling stability[61,62]. Given this, the question of how large a cathode should be in a lithium metal anode cell depends much more on the relationship between the electrolyte and the lithium metal than it does on the transport properties of the cathode.

Appendix

A. Modeling Details

The pseudo two-dimensional (P2D) porous electrode theory (PET) model couples two one-dimensional scales, the particle scale and the electrode scale. We use the open-source implementation in Ref.[41]. The particles are modeled as spheres where the lithium diffusion

flux is governed by Equation 29, shown below.

$$F_s = -D_s \frac{c_s}{c_{s,max}} \left(1 - \frac{c_s}{c_{s,max}}\right) \nabla c_s \tag{29}$$

Boundary conditions are applied such that the diffusion is symmetric and the flux through the surface matches the reaction rate.

$$\nabla F_s|_{r=0} = 0 \qquad \text{and} \qquad F_s|_{r=R_s} = -j \tag{30}$$

The reaction rate at the surface of the particle is governed by the Butler-Volmer equation, shown below.

$$\begin{aligned} j_{cat} &= j_{0,cat} \left(\exp\left[-\frac{\alpha F \eta_{s,cat}}{RT}\right] - \exp\left[\frac{(1-\alpha) F \eta_{s,cat}}{RT}\right] \right) \\ \eta_{s,cat} &= U(c_{s,surf}) - (\phi_{el} - \phi_s) \end{aligned} \tag{31}$$

The exchange current density, $j_{0,cat}$, can be described with

$$j_{0,cat} = k_0 \left(\frac{c_{el}}{c_{el,0}}\right)^{1-\alpha} \left(\frac{c_{s,surf}}{c_{s,max}}\right)^{1-\alpha} \left(1 - \frac{c_{s,surf}}{c_{s,max}}\right)^{\alpha}. \tag{32}$$

The electrochemical potential in active NMC particles, $U(c_s)$, is modeled based on the fit of a C/10 charge of a 28 µm cathode with 55 % porosity and 0.695 mAh cm^{-2}. The fitting equation is shown in Equation 33 and parameters are shown in Table 2.

$$\begin{aligned} U(\hat{c}_s) &= (m_1 - k_1 \hat{c}_s) g(\hat{c}_s, q, p) \\ &\quad + (m_2 - k_2 \hat{c}_s)(1 - g(\hat{c}_s, q, p)) + \frac{r}{\hat{c}_s - s} \\ g(\hat{c}_s, q, p) &= \frac{1}{2} - \frac{1}{\pi} \tan^{-1}\left[(\hat{c}_s - q) \cdot p\right] \\ \hat{c}_s &= \frac{c_s}{c_{s,max}} \end{aligned} \tag{33}$$

The potentials in the solid and electrolyte phases, ϕ_s and ϕ_{el}, are determined implicitly by the equations that govern the current through the phases across the cell. The electric current through the cathode is governed by Ohm's law, shown below.

$$i_s = -\sigma_s (1 - \varepsilon)^{1.5} \nabla \phi_s \tag{34}$$

The electric current through the electrolyte is modeled with

$$i_{el} = \sigma_{el} \varepsilon^{1.5} \left(-\nabla \phi_{el} + \frac{2RT}{F} (1 - t_+^0) f_{therm} \nabla \ln \left[\frac{c_{el}}{c_{el,0}}\right] \right). \tag{35}$$

The conductivity of the electrolyte, σ_{el}, is related to the diffusion coefficient through the Nernst-Einstein equation.

$$\sigma_{el} = D_{el} \frac{c_{el} F^2}{RT} \tag{36}$$

The current in Equation 35 results in the flux of lithium through the electrolyte, according to Equation 37, shown below.

$$F_{el} = -D_{el}\varepsilon^{1.5}\nabla c_{el} - (1 - t_+^0)\frac{i_{el}}{e} \tag{37}$$

where D_{el} is the diffusion coefficient of the dissolved lithium in the electrolyte. As the dissolved lithium flows across the cell and into the cathode particles, equal amounts are dissolving into the electrolyte at the Li-metal surface. This process is governed by the Butler-Volmer equation, except that the exchange current density, $j_{0,an}$, is set constant. In addition, at the anode, we include a film resistance R_{an}. This equation implicitly determines the anode overpotential, $\eta_{s,an}$, from the discharge current and material parameters.

$$\begin{aligned} I_{cell} = j_{0,an}\Bigg(&\exp\left[-\frac{\alpha F}{RT}(\eta_{s,an} + I_{cell}R_{an})\right] \\ &- \exp\left[\frac{(1-\alpha)F}{RT}(\eta_{s,an} + I_{cell}R_{an})\right]\Bigg) \end{aligned} \tag{38}$$

Boundary conditions are applied such that lithium diffusion is contained within the electrolyte and the electric current is contained within the solid phase. These are shown below.

$$\begin{aligned} F_{el}|_{x=x_{an}} &= 0 \qquad & i_{el}|_{x=x_{an}} &= I_{cell} \\ i_s|_{x=x_{sep/cat}} &= 0 & & \\ i_{el}|_{x=x_{cat/cc}} &= 0 \qquad & F_{el}|_{x=cat/cc} &= 0 \end{aligned} \tag{39}$$

The particle and electrode scales are coupled through the mass and charge conservation conditions, shown below.

$$\begin{aligned} 0 &= -\nabla \cdot i_s - eF_R \\ 0 &= -\nabla \cdot i_{el} + eF_R \\ \frac{\partial(\varepsilon c_{el})}{\partial t} &= -\nabla F_{el} + F_R \end{aligned} \tag{40}$$

where F_R is the total reaction flux through all particle surfaces within a modeled volume on the electrode scale, given by

$$F_R = -(1 - \varepsilon_{cat})v_{AM}j_{cat}\frac{3}{R_s}. \tag{41}$$

v_{AM} is the volumetric ratio of the active material in the solid phase of the porous cathode. The necessary parameters are listed in Table 1.

For the purposes of Figure 2, the rate-limiting regions are defined as follows:

- ISD-limited (red): $c_{s,surf} > 0.99c_{s,max}$ at ALL locations within the cathode.

- ILD-limited (blue): $c_{el} < 0.1$ M at ANY location within the cathode, AND $c_{s,surf} < 0.99 c_{s,max}$ at ANY location in the cathode.
- OCT-limited (yellow): $c_{s,surf} < 0.99 c_{s,max}$ at ALL locations in the cathode, AND $c_{el} > 0.1$ M at ALL locations within the cathode.

Table 1: Model Parameters

Cathode		
ε_{cat}	50	%
L_{cat}	50, 100, and 200	µm
σ_s	10	$\mathrm{S\,m^{-1}}$
D_s	$2.6 \cdot 10^{-13}$	$\mathrm{m^2\,s^{-1}}$
$c_{s,max}$	$2.7523 \cdot 10^{28}$	$\mathrm{m^{-3}}$
R_s	5.75	µm
k_0	8.5	$\mathrm{A\,m^{-2\,63}}$
α	0.5	
Anode		
$j_{0,an}$	10	$\mathrm{A\,m^{-2}}$
R_{an}	$6.5 \cdot 10^{-3}$	$\Omega\,\mathrm{m^2}$
α	0.5	
Separator		
ε_{cat}	42	%
L_{sep}	17	µm
Electrolyte		
D_{el}	$2.9 \cdot 10^{-11}$	$\mathrm{m^2\,s^{-1}}$
f_{therm}	1	
t_+^0	0.38	
c_{el} at $t = 0$	1700	$\mathrm{mol\,m^{-3}}$

Table 2: $U(\hat{c}_s)$ fitting parameters

m_1	5.07333784	q	$6.86850722 \cdot 10^{-1}$
k_1	1.97899504	p	6.56174271
m_2	4.24827606	r	$6.02791677 \cdot 10^{-5}$
k_2	$4.47170779 \cdot 10^{-1}$	s	1.00003

B. Solid-Diffusion Limit Model Development

During solid-diffusion limited discharges, the discharge ends when all particle surfaces are full. Consequently, the amount of capacity extracted from the discharge is determined by

the amount of lithium that had entered the particle by the time the particle surface became full. Here we create a simple model to describe how the discharge capacity depends on C-rate in the solid-diffusion region. We will consider a spherical active particle with a constant diffusion coefficient D, a radius R_s, initial concentration $c_{s,0}$, maximum concentration $c_{s,max}$, surface area A, and volume V. Lithium ions enters the particle at a constant flux J, establishing a steady-state diffusion gradient. Diffusion is governed by Fick's second law of diffusion (Equation 42), shown below.

$$\frac{\partial c}{\partial t} = \nabla(D\nabla c) \tag{42}$$

where c is the active particle concentration and t is the time. Expressing Fick's law in spherical coordinates while ignoring angular components yields

$$\frac{\partial c}{\partial t} = \frac{D}{r^2}\frac{\partial}{\partial r}\left(r^2\frac{\partial c}{\partial r}\right) \tag{43}$$

where r is the radial coordinate of the spherical particle. Transforming the variables with $r = \phi R_s$, $t = \tau R_s^2/D$, and $c = u(c_{s,max} - c_{s,0})$ yields

$$\frac{\partial u}{\partial \tau} = \frac{1}{\phi^2}\frac{\partial}{\partial \phi}\left(\phi^2\frac{\partial u}{\partial \phi}\right) \tag{44}$$

The constant flux and steady-state filling results in a uniform filling rate $\dot{\bar{u}}$, shown below.

$$\dot{\bar{u}} = \frac{\partial u}{\partial \tau} = \frac{\partial c}{\partial t}\frac{R_s^2}{D(c_{s,max} - c_{s,0})} = \frac{JAR_s^2}{VD(c_{s,max} - c_{s,0})} \tag{45}$$

Equation 44 is satisfied by

$$u(\phi, \tau) = \dot{\bar{u}}\left(\frac{\phi^2}{6} + \tau\right). \tag{46}$$

The discharge ends when the particle surface is full, corresponding to $u(1, \tau_{end}) = 1$, resulting in the profile given by

$$u_{end}(\phi) = 1 - (1 - \phi^2)\frac{\dot{\bar{u}}}{6}. \tag{47}$$

Equation 47 is plotted with red lines in Figures 12a, b, and c. Integrating over the whole particle (from $\phi = 0$ to $\phi = 1$) gives the final total filling fraction U, shown below.

$$U = 1 - \frac{\dot{\bar{u}}}{9} \tag{48}$$

Unpacking the transformation of this expression yields the final solid-diffusion rate-limit at low currents in Equation 49, shown below.

$$\frac{Q}{M} = Q_M\left(1 - \frac{R_s^2}{9D}R\right) \qquad \text{(sphere)} \tag{49}$$

where Q is the discharge capacity, M is the particle mass, Q_M is the specific capacity of the active material, and R is the C-rate (defined as $R = JA/V(c_{s,max} - c_{s,0})$). Equation 49 is plotted with a red line in Figure 12. A similar process can be used to find the solid-diffusion rate-limit for cylindrical particles with radius R_{cyl} and platelet particles with thickness L_{pl}, shown below.

$$\frac{Q}{M} = Q_M\left(1 - \frac{R_{cyl}^2}{6D}R\right) \qquad \text{(cylinder)} \tag{50}$$

$$\frac{Q}{M} = Q_M\left(1 - \frac{11L_{pl}^2}{24D}R\right) \qquad \text{(plate)} \tag{51}$$

This model results in a capacity decay that is linear with C-rate with a slope that depends on the size, shape, and diffusion coefficient of the particles. This very simple model does not take into account the concentration dependence of the diffusion coefficient, the impact of stress or strain, phase separation in the active material, nor particle swelling[13,64,65]. These are all impacted by the concentration gradient in the particle which, in turn, are impacted by the C-rate. Furthermore, real cathodes contain particles with a distribution of sizes and shapes that will experience very different local C-rates while the cell as a whole is discharged at a constant current. Nevertheless, this general form (see Equation 52) is used to fit the solid-diffusion limited region of the data in order to somewhat match earlier work on rate performance[35,36,39]. However, the physical meaning of the two fitting parameters, τ and n, are reinterpreted. τ is the time constant of diffusion in the active particle, given the particle shape/size distribution and diffusion coefficient. n represents the deviation from this idealized diffusion model.

$$\frac{Q}{M} = Q_M\big(1 - (\tau R)^n\big) \tag{52}$$

Figure 12 shows the internal concentration profiles and the rate performance of a single spherical particle with a constant diffusion coefficient. The markers represent results from numerical simulations and the red lines show the analytical solutions in Equations 47 and 49. The simulations were performed using the open-source simulation program MPET in Ref.[41].

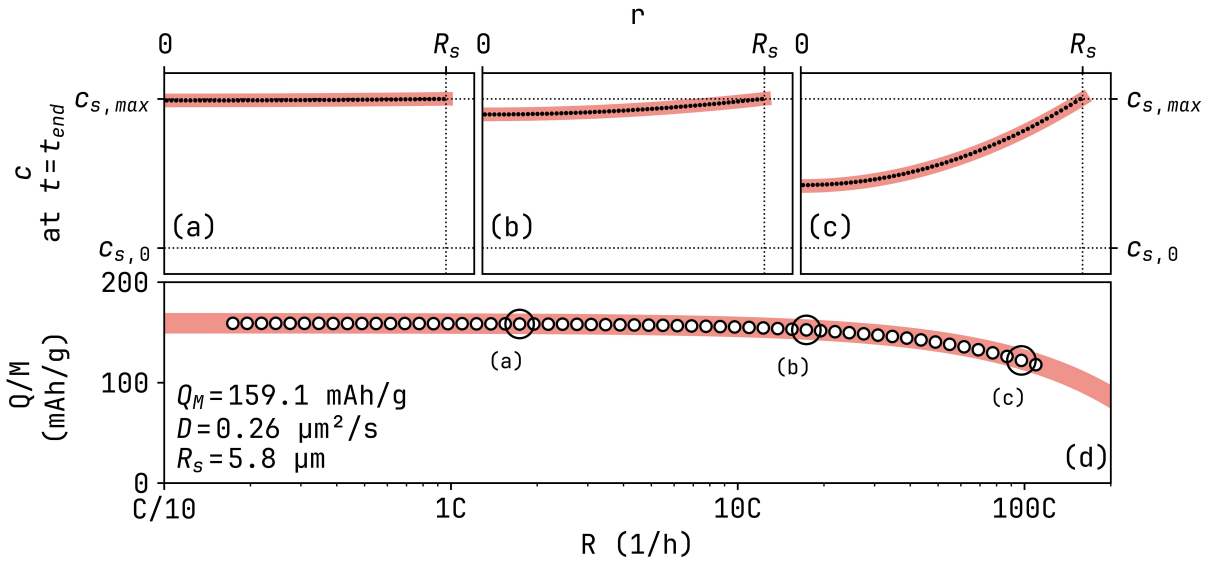

Figure 12: Results from simulated single spherical particle discharges together with analytical solutions. (d) shows the single particle discharge capacities as a function of C-rate. (a-c) show the internal lithium distribution at end of discharge. The black markers in (a-c) and white markers in (d) represent results from numerical simulations. The red lines in (a-c) and (d) represent the analytical solution in Equations 47 and 49, respectively.

C. Impact of Concentration Profile on the OCT limit

In this section, we derive expressions for the OCT potential, ΔV_{OCT}, given the concentration profiles developed in the previous section. We limit the derivation to the |MZR cell profile. We assemble the profile from the expressions for the separator in Equation 14, the MZR cathode in Equation 12, the transformations in Equations 18 and 23, as well as defining unitless time as $\theta = x_r / L_{cat}$.

$$\frac{c(x)}{c_0} = \begin{cases} 1 + 2\dfrac{I}{I_d}\left[\theta - \nu_{cat}\left(\theta^2 - \dfrac{\theta}{2}\right) - \nu_{sep}\left(\theta + \dfrac{\kappa_{sep}}{2}\right) - \dfrac{x - x_{sc}}{L_{sep}}\right] & x_{as} \leq x < x_{sc} \\ 1 + 2\dfrac{I}{I_d}\left[\theta - \nu_{cat}\left(\theta^2 - \dfrac{\theta}{2}\right) - \nu_{sep}\left(\theta + \dfrac{\kappa_{sep}}{2}\right) - \dfrac{x - x_{sc}}{L_{cat}}\right] & x_{sc} \leq x < x_{sc} + x_r \\ 1 - 2\dfrac{I}{I_d}\left[\nu_{cat}\left(\theta^2 - \dfrac{\theta}{2}\right) + \nu_{sep}\left(\theta + \dfrac{\kappa_{sep}}{2}\right)\right] & x_{sc} + x_r \leq x < x_{cc} \end{cases} \tag{53}$$

C.1. Ohmic Potential

Moving Zone Reaction systems were studied and developed mathematically by Newman et al. in 1995[53]. Their treatment focuses on the Ohmic contribution of the electrolyte. Here,

we include the Ohmic potential of the conductive matrix as well, shown below.

$$\Delta\Phi_{Ohm} = \int_{-L_{sep}}^{x_r} i_{el}\rho_{el}\ \mathrm{d}x + \int_{x_r}^{L_{cat}} i_s\rho_s\ \mathrm{d}x = IL_{sep}\rho_{el,sep} + Ix_r\rho_{el,cat} + I(L_{cat} - x_r)\rho_s \quad (54)$$

where L_{sep} and L_{cat} are the separator and cathode thicknesses. This assumes uniform and constant ionic resistivities in the separator and cathode. Given that the resistivity is concentration-dependent[66], this assumption applies in the absence of steep concentration gradients. The location of the reaction zone, x_r, can be expressed with

$$x_r = \frac{It}{Q_V} \quad (55)$$

Inserting equation 55 into Equation 54 yields

$$\Delta\Phi_{Ohm} = I(L_{sep}\rho_{el,sep} + L_{cat}\rho_{s,cat}) + \frac{I^2t}{Q_V}(\rho_{el,cat} - \rho_{s,cat}) \quad (56)$$

The Ohmic contribution is the largest at end of discharge, when $It_{end} = L_{cat}Q_V$, shown below.

$$\Delta\Phi_{Ohm}^{end} = I(L_{sep}\rho_{el,sep} + L_{cat}\rho_{el,cat}) \quad (57)$$

If the Ohmic contribution exceeds the margin voltage, $\Delta V_{margin} = V_0 - V_{thresh}$, the discharge will reach the threshold voltage, V_{thresh}, before the reaction zone reaches the current collector. The capacity beyond this point will remain unutilized. This limits discharges to currents below I_{crit}^{OCT}, shown below.

$$I_{crit}^{OCT} = \frac{\Delta V_{margin}}{L_{sep}\rho_{el,sep} + L_{cat}\rho_{el,cat}} \quad (58)$$

These expressions assumes uniform resistivities. However, ionic resistivities are inversely proportional to concentration (in dilute solutions) according to the Nernst-Einstein relation, shown below[67].

$$\rho_{el} = \frac{RT}{n^2F^2D_{el}c} \quad (59)$$

where R is the gas constant and F is the Faraday constant. We insert this expression into equation 54, shown below.

$$\Delta\Phi_{Ohm} = I\frac{RT}{n^2F^2}\left(\frac{1}{D_{sep}}\int_{x_{as}}^{x_{sc}} \frac{1}{c(x)}\ \mathrm{d}x + \frac{1}{D_{cat}}\int_{x_{sc}}^{x_{sc}+x_r} \frac{1}{c(x)}\ \mathrm{d}x\right) + I(L_{cat} - x_r)\rho_{s,cat} \quad (60)$$

Inserting the concentration profile of the |MZR cell in Equation 53 yields the Ohmic contribution shown below.

$$\Delta\Phi_{Ohm} = \frac{RT}{nF}\ln\left(1 + 2\frac{I}{I_d}\left[\frac{\theta + \kappa_{sep}}{1 - \frac{I}{I_d}\left[\theta^2(1 - v_{sep}) + (\kappa_{sep} + 2\theta)\nu_{sep}\right]}\right]\right) + I\rho_{s,cat}L_{cat}(1 - \theta) \quad (61)$$

The logarithm approaches infinity as the denominator approaches zero. This reflects the fact that the resistivity approaches infinity as the electrolyte concentration is depleted. In contrast to the |MZR cell, the Ohmic potential in the |UR cell is not expected to diverge as the electrolyte is depleted. This is a consequence of the uniform reaction allowing for more reaction locations that can accelerate to compensate for the shortfall at depleted regions.

C.2. Concentration and Anode Overpotentials

Both the concentration overpotential η_{el} and the anode surface overpotential η_{an} depend on the electrolyte concentrations at the anode and reaction zone. We approximate the oxidation at the anode with the Butler-Volmer equation[67]. For simplicity, we ignore the reduction term. The concentration at the anode is found in equation 53 with $c_{as} = c(x_{as})$. This yields the anode surface overpotential shown below.

$$\eta_{an} = \frac{RT}{nF} \ln\left(\frac{I}{k_0 (c_{as}/c_0)^{\alpha}}\right) \tag{62}$$

$$= \frac{RT}{nF}\left[\ln\frac{I}{k_0} - \alpha \ln\left(1 + \frac{I}{I_d}\left[(\theta(2-\theta) + \kappa_{sep})(1 - \upsilon_{sep}) + \kappa_{sep}\right]\right)\right] \tag{63}$$

where I is the cell current, k_0 is the rate constant at an electrolyte concentration of c_0, and α is the symmetry factor. The concentration overpotential is here simplified with that of a dilute solution and we ignore the thermodynamic factor, shown below.

$$\eta_{el} = -\frac{RT}{nF} \ln\left(\frac{c_r}{c_{an}}\right) \tag{64}$$

$$= \frac{RT}{nF} \ln\left(1 + 2\frac{I}{I_d}\left[\frac{\theta + \kappa_{sep}}{1 - \frac{I}{I_d}\left[\theta^2(1-\upsilon_{sep}) + (\kappa_{sep} + 2\theta)\nu_{sep}\right]}\right]\right) \tag{65}$$

C.3. End of Discharge

The Ohmic/charge-transfer critical current is the current where the cell polarization exceeds the margin voltage ($\Delta V_{margin} = U - V_{thresh}$) before the end of discharge. The size of the cell voltage at end of discharge is found by inserting $\theta = 1$ into on equations 62, 64, and 61, shown below.

$$\eta_{an}^{end} = \frac{RT}{nF}\left[\ln\frac{I}{k_0} - \alpha \ln\left(1 + 2\frac{I}{I_{crit}^{ILD}}\left[\frac{1 + \kappa_{sep}}{1 + \nu_{sep}(1 + \kappa_{sep})} - \frac{1}{2}\right]\right)\right] \tag{66}$$

$$\eta_{el}^{end} = \frac{RT}{nF} \ln\left(1 + 2\frac{I}{I_{crit}^{ILD} - I}\left[\frac{1 + \kappa_{sep}}{1 + \nu_{sep}(1 + \kappa_{sep})}\right]\right) \tag{67}$$

$$\Delta\Phi_{Ohm}^{end} = \frac{RT}{nF} \ln\left(1 + 2\frac{I}{I_{crit}^{ILD} - I}\left[\frac{1 + \kappa_{sep}}{1 + \nu_{sep}(1 + \kappa_{sep})}\right]\right) \tag{68}$$

C.4. Low Currents

At currents low enough for the concentration gradients to be negligible (where $I << I_{crit}^{ILD}$, $\ln(1+y) \approx y$, and $c(x) \approx c_0$), these potentials can be expressed as

$$\eta_{an}^{low} = \frac{RT}{nF} \ln \frac{I}{k_0} - I\alpha \left(\rho_{el,cat} L_{cat} (1 - v_{sep}) \left[\theta - \frac{\theta^2}{2} \right] + \rho_{el,sep} L_{sep} \left[1 - \frac{v_{sep}}{2} \right] \right) \tag{69}$$

$$\eta_{el}^{low} = I \left[\theta L_{cat} (\rho_{el,cat} - \rho_{s,cat}) + \rho_{el,sep} L_{sep} + \rho_{s,cat} L_{cat} \right] \tag{70}$$

$$\Delta\Phi_{Ohm}^{low} = I \left[\theta L_{cat} (\rho_{el,cat} - \rho_{s,cat}) + \rho_{el,sep} L_{sep} + \rho_{s,cat} L_{cat} \right] \tag{71}$$

Inserting these into the expression for the cell voltage shows us the cell voltage in the plateau region of the discharge curve at low currents, shown below.

$$\begin{aligned} V_{cell}^{low} =& U + \eta_r \\ &+ \frac{RT}{nF} \ln \frac{I}{k_0} \\ &+ I\theta L_{cat} \left(\rho_{el,cat} \left[2 - \alpha(1 - v_{sep}) \right] - 2\rho_{s,cat} \right) \\ &+ I \frac{\theta^2}{2} L_{cat} \rho_{el,cat} (1 - v_{sep}) \alpha \\ &+ I \left(2\rho_{s,cat} L_{cat} + \rho_{el,sep} L_{sep} \left[2 - \alpha \left(1 - \frac{v_{sep}}{2} \right) \right] \right) \end{aligned} \tag{72}$$

The cell voltage increases quadratically with time and both linearly and logarithmically with current. This expression can be parameterized as

$$V_{cell}^{low} = A + B \ln(I) + I(C\theta^2 + D\theta + E) \tag{73}$$

We use this fitting function to fit a region of the discharge curve. We then extrapolate the fitted voltage to the threshold voltage to find the current at which the polarization exceeds the margin voltage. This serves as an upper limit of the OCT critical current I_{crit}^{OCT} as long as I is below the ILD critical current.

D. Experimental Data

D.1. Sample Data

Table 3: Sample data grouped by cathode sheet. Each row corresponds to all cathodes punched from the same set of sheet with equal loading, although with different degrees of calendering. The numbers show the geometric averages with the multiplicative standard deviation in the parenthesis, such that $x(g)$ denotes the interval x/g to xg. The active material loading is calculated by multiplying the measured cathode mass with the supplied active material mass ratios of the sheets (90 % for NMC and 88 % for LFP). The nominal capacity is average discharge capacity of the C/10 formation cycles and final cycles, divided by the cathode area.

Cathode Material	Cells #	#	Active Material Loading ($\mathrm{mg\,cm^{-3}}$)	Nominal Capacity ($\mathrm{\mu m{\cdot}mAh\,cm^{-2}}$)
LFP	86	20	3.60(1.02)	0.585(1.02)
		19	6.74(1.03)	1.08(1.03)
		16	10.7(1.03)	1.70(1.03)
		16	13.6(1.04)	2.15(1.04)
		15	16.7(1.08)	2.65(1.08)
NMC	58	16	4.76(1.04)	0.709(1.03)
		16	9.10(1.03)	1.38(1.03)
		12	18.2(1.04)	2.72(1.03)
		12	26.6(1.07)	3.98(1.07)
		18	36.6(1.04)	5.37(1.03)

Table 4: Sample data grouped by degree of calendering. Each row corresponds to all cathodes calendered to the same target porosity, although with different loading. The numbers show the geometric averages with the multiplicative standard deviation in the parenthesis, such that $x(g)$ represents the range from x/g to xg. The porosity is calculated from the cathode mass and thickness, according to the method described in Section 3.2. The volumetric nominal capacity is the areal capacity divided by cathode thickness.

Cathode Material	Cells #	#	Porosity (%)	Nominal Capacity ($\mathrm{\mu m{\cdot}mAh\,cm^{-3}}$)
LFP	86	20	54.6(1.01)	209(1.04)
		38	43.1(1.17)	256(1.13)
		28	23.5(1.11)	352(1.03)
NMC	58	20	50.7(1.04)	259(1.04)
		19	25.9(1.09)	383(1.03)
		19	18.9(1.15)	428(1.05)

Table 5: Measured proportionality constants and optimized thickness at 1 C for ILD-limited LFP and NMC cathodes of varying porosity. Values are reported as geometric means; parenthetical values indicate the geometric standard deviation (multiplicative uncertainty), such that $x(g)$ denotes the interval x/g to xg.

Active Material	ε_{cat} (%)	$Q_{V,s}$ ($\mathrm{mAh\,cm^{-3}}$)	$L_{cat}I_{crit}^{ILD}$ ($\mu\mathrm{m{\cdot}mA\,cm^{-2}}$)	$\varepsilon_{cat}^{-1}L_{cat}I_{crit}^{ILD}$ ($\mu\mathrm{m{\cdot}mA\,cm^{-2}}$)
LFP	24.5(1.07)	461(1.01)	704(1.25)	2878(1.23)
NMC	20.3(1.11)	527(1.02)	642(1.16)	3169(1.20)
NMC	27.4(1.06)	517(1.01)	803(1.14)	2933(1.13)
NMC	49.1(1.02)	523(1.02)	1212(1.08)	2468(1.07)
Active Material	ε_{cat} (%)	$Q_{V,s}$ ($\mathrm{mA\,h\,cm^{-3}}$)	$Q_A^2R_{crit}^{ILD}$ ($\mathrm{h^{-1}{\cdot}(mAh\,cm^{-2})^2}$)	$\varepsilon_{cat}^{-1}(1-\varepsilon_{cat})^{-1}Q_A^2R_{crit}^{ILD}$ ($\mathrm{h^{-1}{\cdot}(mA\,h\,cm^{-2})^2}$)
LFP	24.5(1.07)	461(1.01)	15(1.24)	83(1.23)
NMC	20.3(1.11)	527(1.02)	27(1.17)	167(1.22)
NMC	27.4(1.06)	517(1.01)	30(1.13)	152(1.13)
NMC	49.1(1.02)	523(1.02)	32(1.08)	129(1.08)
Active Material	ε_{cat} (%)	$Q_{V,s}$ ($\mathrm{mAh\,cm^{-3}}$)	L_{opt} at 1 C (μm)	Q_A at L_{opt} ($\mathrm{mAh\,cm^{-2}}$)
LFP	24.5(1.07)	461(1.01)	142(1.12)	3.907(1.11)
NMC	20.3(1.11)	527(1.02)	124(1.07)	5.192(1.08)
NMC	27.4(1.06)	517(1.01)	146(1.07)	5.488(1.06)
NMC	49.1(1.02)	523(1.02)	214(1.04)	5.678(1.04)

D.2. Discharge Curves, Rate Performance, and Critical Currents

Figure 13: Supplemental Figures A-D show the experimental data from all 86 LFP|Li-metal coin cells (A and B) and all 58 NMC|Li-metal coin cells (C and D). Each panel in Figures A and C show the discharge curves, applied voltage vs discharged capacity throughout a discharge, of the rate performance experiment of a Li-metal anode coin cell, described in Section 3.3. Each panel in Figures B and D show the rate performance of a coin cell, the discharge capacity at the end of discharge vs discharge current. The sharp capacity drop is marked with a vertical purple line. The grid is organized in 2x2 groups of cathodes punched from the same sheet. These groups are ordered with ascending cathode thickness from left to right, and with ascending porosity from bottom to top. The cathode thickness and porosity are listed in the top right corner of each panel and are plotted in the panel on the top right. The markers represent groups of cells with similar porosity. The colors of the markers and of the panels correspond to the type of critical current (teal for ILD, yellow for OCT, and red for ISD). They are determined by looking at both the discharge curves and the rate performance.

OCT The capacity drops sharply and the applied voltage reaches the threshold without diverging.

ILD The capacity drops sharply and the applied voltage diverges.

ISD/PT There is no sharp capacity drop, but a slow decrease to zero at high currents.

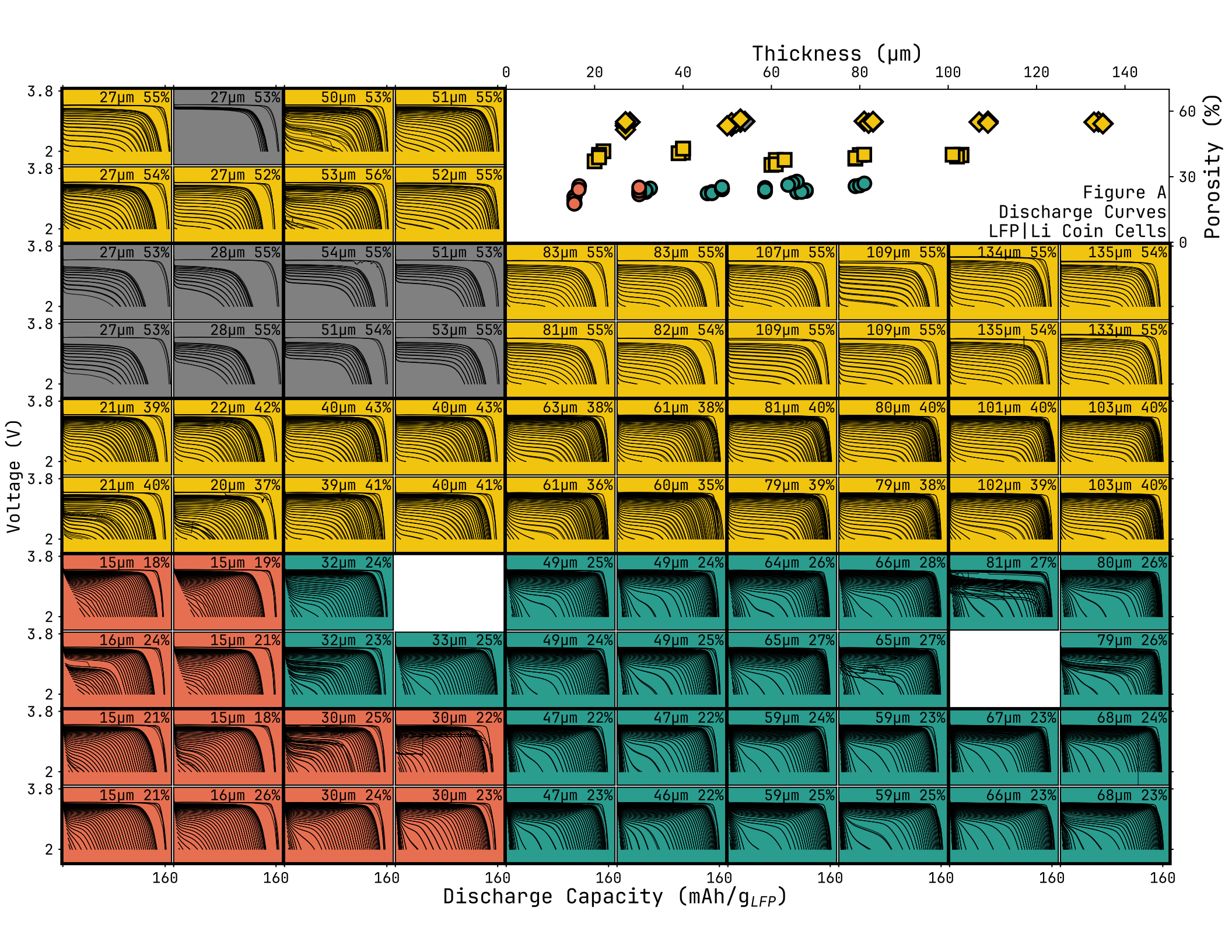
Thickness (µm)
0
20
40
60
80
100
120
140
Porosity (%)
0
30
60
Figure A
Discharge Curves
LFP|Li Coin Cells
Voltage (V)
3.8
2
Discharge Capacity (mAh/g$_{LFP}$)
160
27µm 55%
27µm 53%
50µm 53%
51µm 55%
27µm 54%
27µm 52%
53µm 56%
52µm 55%
27µm 53%
28µm 55%
54µm 55%
51µm 53%
83µm 55%
83µm 55%
107µm 55%
109µm 55%
134µm 55%
135µm 54%
27µm 53%
28µm 55%
51µm 54%
53µm 55%
81µm 55%
82µm 54%
109µm 55%
109µm 55%
135µm 54%
133µm 55%
21µm 39%
22µm 42%
40µm 43%
40µm 43%
63µm 38%
61µm 38%
81µm 40%
80µm 40%
101µm 40%
103µm 40%
21µm 40%
20µm 37%
39µm 41%
40µm 41%
61µm 36%
60µm 35%
79µm 39%
79µm 38%
102µm 39%
103µm 40%
15µm 18%
15µm 19%
32µm 24%
49µm 25%
49µm 24%
64µm 26%
66µm 28%
81µm 27%
80µm 26%
16µm 24%
15µm 21%
32µm 23%
33µm 25%
49µm 24%
49µm 25%
65µm 27%
65µm 27%
79µm 26%
15µm 21%
15µm 18%
30µm 25%
30µm 22%
47µm 22%
47µm 22%
59µm 24%
59µm 23%
67µm 23%
68µm 24%
15µm 21%
16µm 26%
30µm 24%
30µm 23%
47µm 23%
46µm 22%
59µm 25%
59µm 25%
66µm 23%
68µm 23%

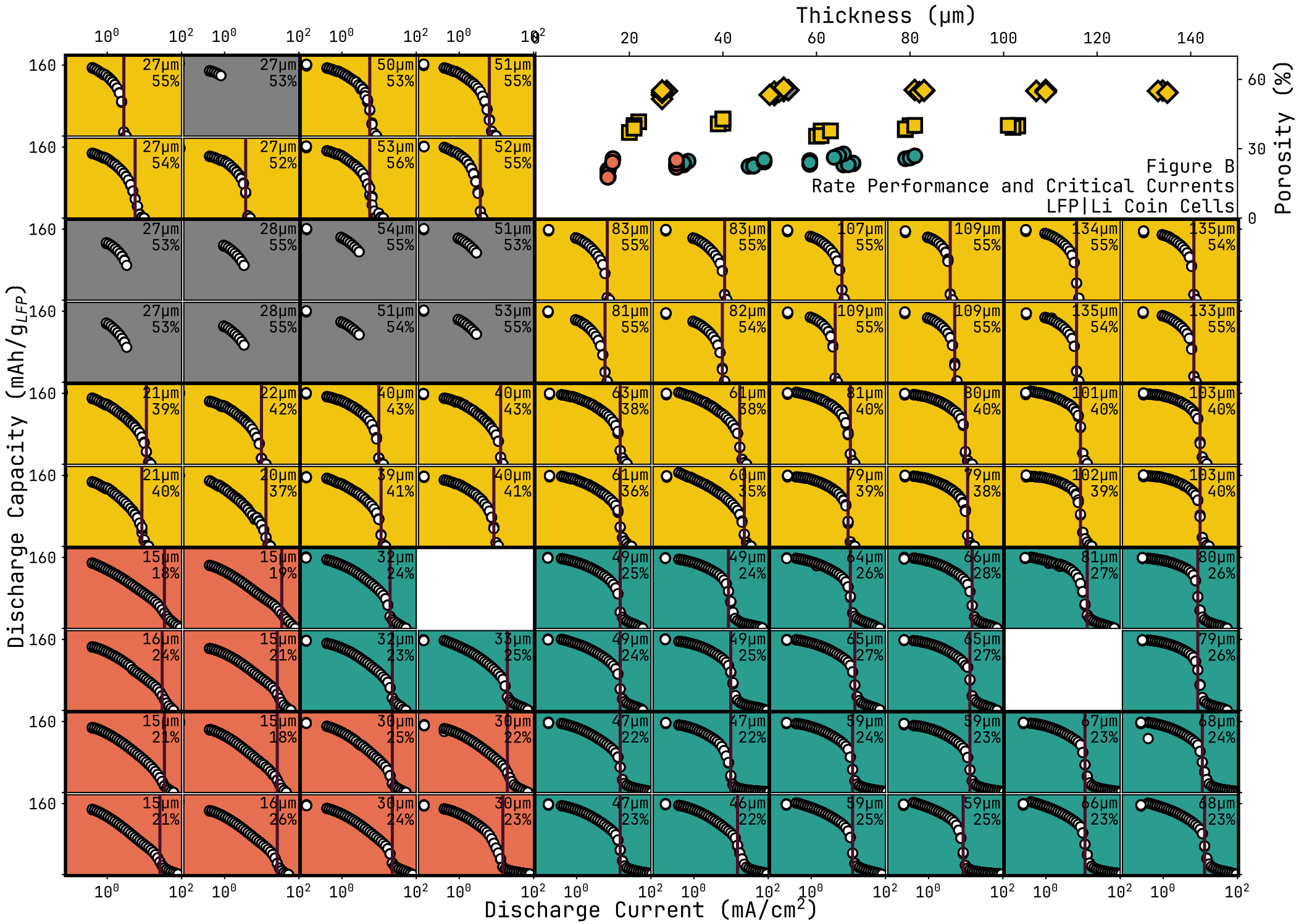
Thickness (µm)
Porosity (%)
Figure B
Rate Performance and Critical Currents
LFP|Li Coin Cells
Discharge Capacity (mAh/g$_{LFP}$)
Discharge Current (mA/cm^2)

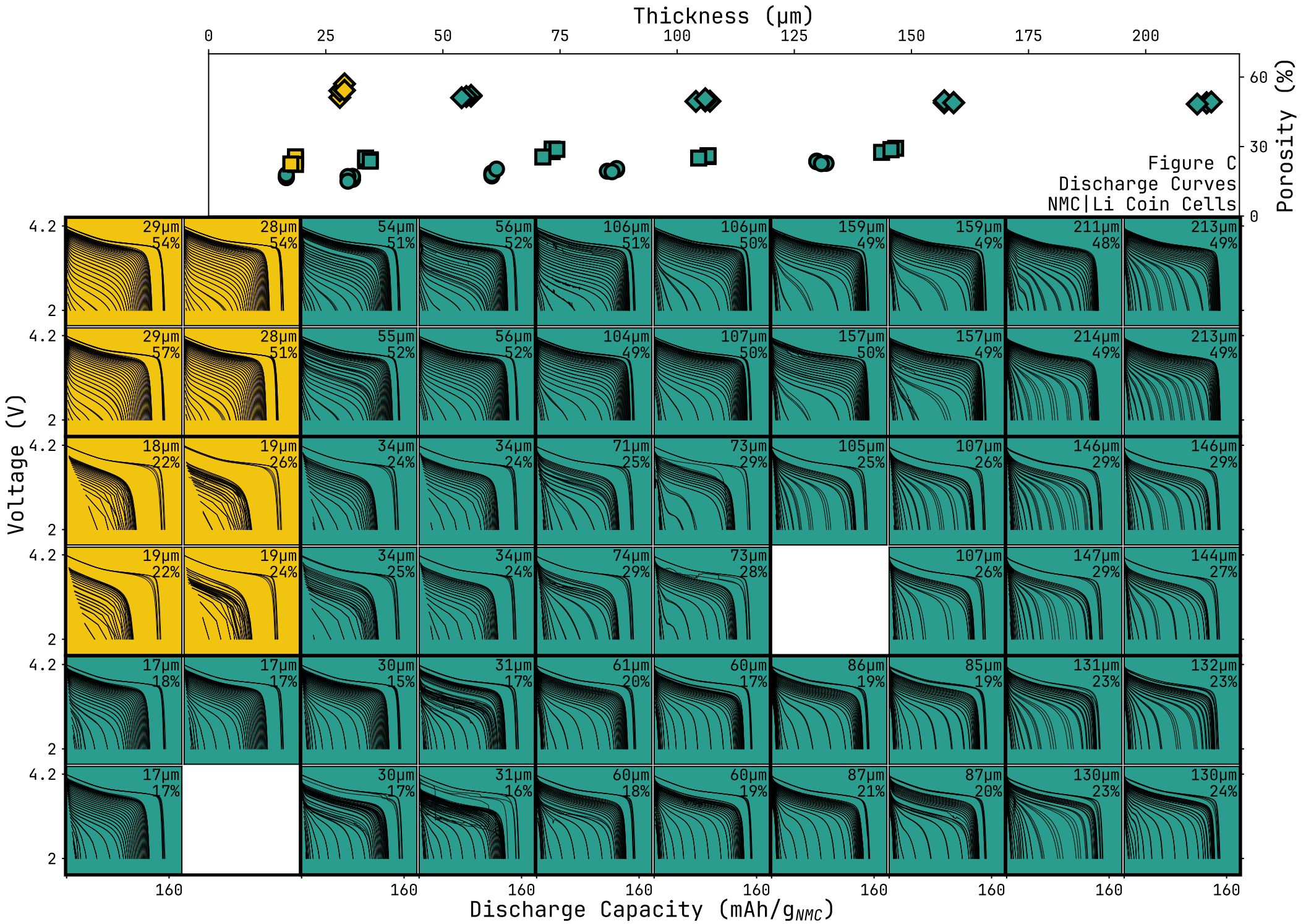
Thickness (µm)
0
25
50
75
100
125
150
175
200
Porosity (%)
60
30
0
Figure C
Discharge Curves
NMC|Li Coin Cells
Voltage (V)
4.2
2
29µm 54%
28µm 54%
54µm 51%
56µm 52%
106µm 51%
106µm 50%
159µm 49%
159µm 49%
211µm 48%
213µm 49%
29µm 57%
28µm 51%
55µm 52%
56µm 52%
104µm 49%
107µm 50%
157µm 50%
157µm 49%
214µm 49%
213µm 49%
18µm 22%
19µm 26%
34µm 24%
34µm 24%
71µm 25%
73µm 29%
105µm 25%
107µm 26%
146µm 29%
146µm 29%
19µm 22%
19µm 24%
34µm 25%
34µm 24%
74µm 29%
73µm 28%
107µm 26%
147µm 29%
144µm 27%
17µm 18%
17µm 17%
30µm 15%
31µm 17%
61µm 20%
60µm 17%
86µm 19%
85µm 19%
131µm 23%
132µm 23%
17µm 17%
30µm 17%
31µm 16%
60µm 18%
60µm 19%
87µm 21%
87µm 20%
130µm 23%
130µm 24%
160
Discharge Capacity (mAh/g$_{NMC}$)

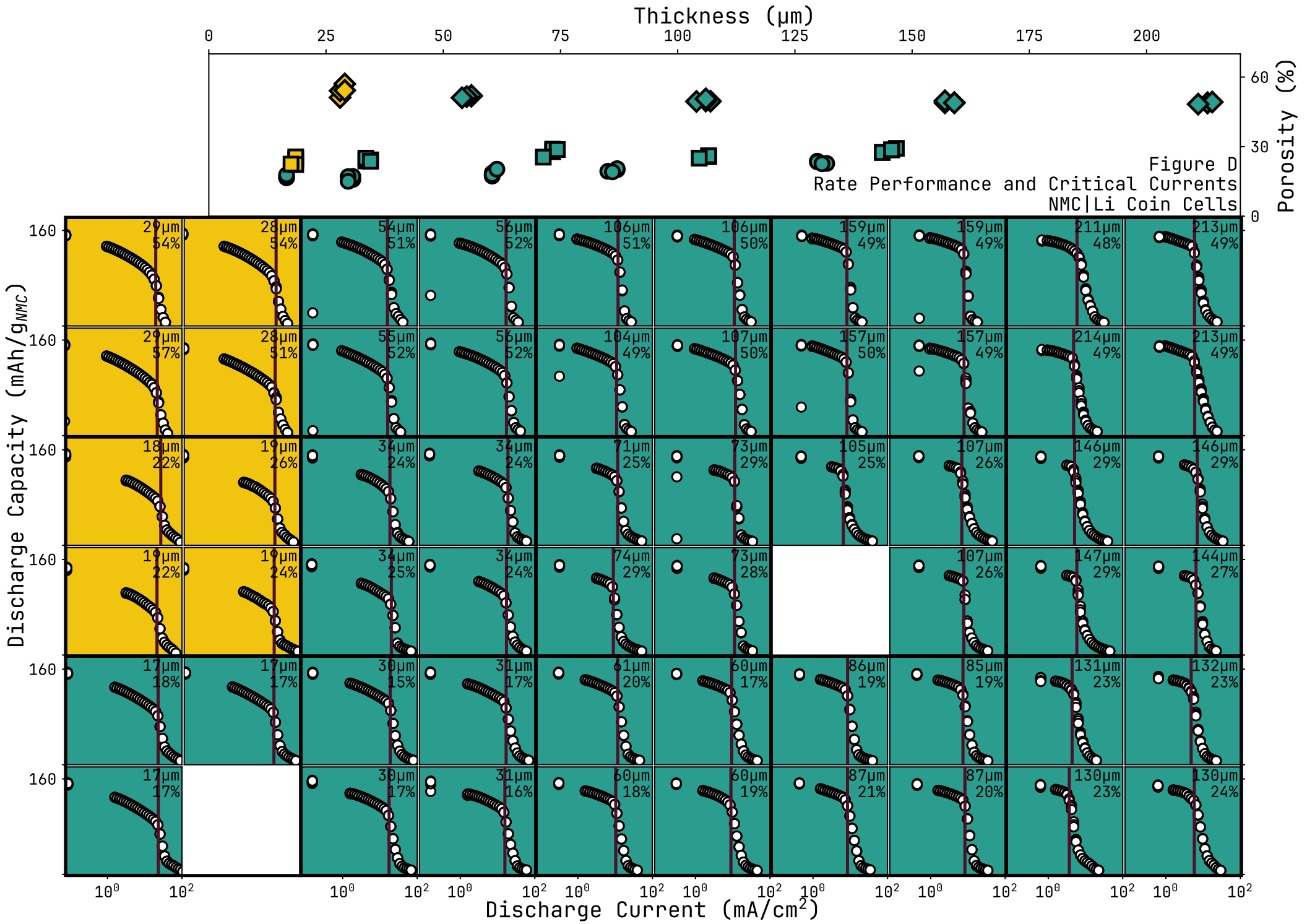
Thickness (µm)
0
25
50
75
100
125
150
175
200
Porosity (%)
0
30
60
Figure D
Rate Performance and Critical Currents
NMC|Li Coin Cells
Discharge Capacity (mAh/g$_{NMC}$)
160
Discharge Current (mA/cm^2)
10^0
10^2
29µm 54%
28µm 54%
54µm 51%
56µm 52%
106µm 51%
106µm 50%
159µm 49%
159µm 49%
211µm 48%
213µm 49%
29µm 57%
28µm 51%
55µm 52%
56µm 52%
104µm 49%
107µm 50%
157µm 50%
157µm 49%
214µm 49%
213µm 49%
18µm 22%
19µm 26%
34µm 24%
34µm 24%
71µm 25%
73µm 29%
105µm 25%
107µm 26%
146µm 29%
146µm 29%
19µm 22%
19µm 24%
34µm 25%
34µm 24%
74µm 29%
73µm 28%
107µm 26%
147µm 29%
144µm 27%
17µm 18%
17µm 17%
30µm 15%
31µm 17%
61µm 20%
60µm 17%
86µm 19%
85µm 19%
131µm 23%
132µm 23%
17µm 17%
30µm 17%
31µm 16%
60µm 18%
60µm 19%
87µm 21%
87µm 20%
130µm 23%
130µm 24%

References

[1] Martin Brischetto, Sicen Yu, Jun Liu, Jie Xiao, and Jihui Yang. On rate-limiting mechanisms in NMC cathodes: The interplay of low and high current constraints. *J. Electrochem. Soc.*, 172(4):40531, April 2025.

[2] Yaxiang Lu, Xiaohui Rong, Yong-Sheng Hu, Liquan Chen, and Hong Li. Research and development of advanced battery materials in China. *Energy Storage Mater.*, 23:144–153, December 2019.

[3] Jun Liu, Zhenan Bao, Yi Cui, Eric J. Dufek, John B. Goodenough, Peter Khalifah, Qiuyan Li, Bor Yann Liaw, Ping Liu, Arumugam Manthiram, Y. Shirley Meng, Venkat R. Subramanian, Michael F. Toney, Vilayanur V. Viswanathan, M. Stanley Whittingham, Jie Xiao, Wu Xu, Jihui Yang, Xiao-Qing Yang, and Ji-Guang Zhang. Pathways for practical high-energy long-cycling lithium metal batteries. *Nat. Energy*, 4(3):180–186, February 2019.

[4] Arno Kwade, Wolfgang Haselrieder, Ruben Leithoff, Armin Modlinger, Franz Dietrich, and Klaus Droeder. Current status and challenges for automotive battery production technologies. *Nat. Energy*, 3(4):290–300, April 2018.

[5] Yudi Kuang, Chaoji Chen, Dylan Kirsch, and Liangbing Hu. Thick electrode batteries: Principles, opportunities, and challenges. *Adv. Energy Mater.*, 9(33):1901457, September 2019.

[6] Jingyi Wu, Xiao Zhang, Zhengyu Ju, Lei Wang, Zeyu Hui, Karthik Mayilvahanan, Kenneth J. Takeuchi, Amy C. Marschilok, Alan C. West, Esther S. Takeuchi, and Guihua Yu. From fundamental understanding to engineering design of high-performance thick electrodes for scalable energy-storage systems. *Adv. Mater.*, 33(26):2101275, July 2021.

[7] Christian Heubner, Kristian Nikolowski, Sebastian Reuber, Michael Schneider, Mareike Wolter, and Alexander Michaelis. Recent insights into rate performance limitations of Li-ion batteries. *Batteries Supercaps*, 4(2):268–285, February 2021.

[8] Chenxi Lu, Weixin Wu, Lujing Wang, Ruiyuan Tian, and Fei Du. Thick electrode for energy storage systems: A facile strategy towards high energy density Li ion batteries. *Next Mater.*, 4:100170, July 2024.

[9] M. Doyle and J. Newman. Analysis of capacity-rate data for lithium batteries using simplified models of the discharge process. *J. Appl. Electrochem.*, 27(7):846–856, 1997.

[10] Kaoru Dokko, Natsuko Nakata, and Kiyoshi Kanamura. High rate discharge capability of single particle electrode of LiCoO2. *J. Power Sources*, 189(1):783–785, April 2009.

[11] Shao-Ling Wu, Wei Zhang, Xiangyun Song, Alpesh K. Shukla, Gao Liu, Vincent Battaglia, and Venkat Srinivasan. High rate capability of Li(Ni $_{1/3}$ Mn $_{1/3}$ Co $_{1/3}$)O $_{2}$ electrode for Li-ion batteries. *J. Electrochem. Soc.*, 159(4):A438, 2012.

[12] Fangming Jiang and Peng Peng. Elucidating the performance limitations of lithium-ion batteries due to species and charge transport through five characteristic parameters. *Sci. Rep.*, 6(1):32639, September 2016.

[13] Yang Bai, Ying Zhao, Wei Liu, and Bai-Xiang Xu. Two-level modeling of lithium-ion batteries. *J. Power Sources*, 422:92–103, May 2019.

[14] Todd R. Ferguson and Martin Z. Bazant. Nonequilibrium thermodynamics of porous electrodes. *J. Electrochem. Soc.*, 159(12):A1967–A1985, 2012.

[15] Jongwoo Lim, Yiyang Li, Daan Hein Alsem, Hongyun So, Sang Chul Lee, Peng Bai, Daniel A. Cogswell, Xuzhao Liu, Norman Jin, Young-sang Yu, Norman J. Salmon, David A. Shapiro, Martin Z. Bazant, Tolek Tyliszczak, and William C. Chueh. Origin and hysteresis of lithium compositional spatiodynamics within battery primary particles. *Science*, 353(6299):566–571, August 2016.

[16] Peng Bai and Martin Z. Bazant. Charge transfer kinetics at the solid–solid interface in porous electrodes. *Nat. Commun.*, 5(1):3585, April 2014.

[17] William Tiedemann and John Newman. Maximum effective capacity in an ohmically limited porous electrode. *J. Electrochem. Soc.*, 122(11):1482–1485, November 1975.

[18] Nobuhiro Ogihara, Yuichi Itou, Tsuyoshi Sasaki, and Yoji Takeuchi. Impedance spectroscopy characterization of porous electrodes under different electrode thickness using a symmetric cell for high-performance lithium-ion batteries. *J. Phys. Chem. C*, 119(9):4612–4619, March 2015.

[19] Stephen J. Harris, Adam Timmons, Daniel R. Baker, and Charles Monroe. Direct in situ measurements of Li transport in Li-ion battery negative electrodes. *Chem. Phys. Lett.*, 485:265–274, January 2010.

[20] Kevin G. Gallagher, Stephen E. Trask, Christoph Bauer, Thomas Woehrle, Simon F. Lux, Matthias Tschech, Peter Lamp, Bryant J. Polzin, Seungbum Ha, Brandon Long, Qingliu Wu, Wenquan Lu, Dennis W. Dees, and Andrew N. Jansen. Optimizing areal capacities through understanding the limitations of lithium-ion electrodes. *J. Electrochem. Soc.*, 163(2):A138–A149, 2016.

[21] Fan Wang and Ming Tang. A quantitative analytical model for predicting and optimizing the rate performance of battery cells. *Cell Rep. Phys. Sci.*, 1(9):100192, September 2020.

[22] Karnail B. Singh and Mahesh S. Tirumkudulu. Cracking in drying colloidal films. *Phys. Rev. Lett.*, 98(21):218302, May 2007.

[23] Rakesh Elango, Arnaud Demortière, Vincent De Andrade, Mathieu Morcrette, and Vincent Seznec. Thick binder-free electrodes for Li–ion battery fabricated using templating approach and spark plasma sintering reveals high areal capacity. *Adv. Energy Mater.*, May 2018.

[24] Sang-Hoon Park, Paul J. King, Ruiyuan Tian, Conor S. Boland, João Coelho, Chuanfang Zhang, Patrick McBean, Niall McEvoy, Matthias P. Kremer, Dermot Daly, Jonathan N. Coleman, and Valeria Nicolosi. High areal capacity battery electrodes enabled by segregated nanotube networks. *Nat. Energy*, 4(7):560–567, June 2019.

[25] Lorenzo Zolin, Marion Chandesris, Willy Porcher, and Bernard Lestriez. An innovative process for ultra-thick electrodes elaboration: Toward low-cost and high-energy batteries. *Energy Technol.*, 7(5):1900025, May 2019.

[26] Yangfan Zhang, Fuzhen Li, Kang Yang, Xiu Liu, Yaoguang Chen, Zhengqi Lao, Kancheng Mai, and Zishou Zhang. Polymer molecular engineering enables rapid electron/ion transport in ultra-thick electrode for high-energy-density flexible lithium-ion battery. *Adv. Funct. Mater.*, 31(19):2100434, May 2021.

[27] Feifei Shi, Allen Pei, David Thomas Boyle, Jin Xie, Xiaoyun Yu, Xiaokun Zhang, and Yi Cui. Lithium metal stripping beneath the solid electrolyte interphase. *Proc. Natl. Acad. Sci.*, 115(34):8529–8534, August 2018.

[28] David T. Boyle, Yuzhang Li, Allen Pei, Rafael A. Vilá, Zewen Zhang, Philaphon Sayavong, Mun Sek Kim, William Huang, Hongxia Wang, Yunzhi Liu, Rong Xu, Robert Sinclair, Jian Qin, Zhenan Bao, and Yi Cui. Resolving current-dependent regimes of electroplating mechanisms for fast charging lithium metal anodes. *Nano Lett.*, 22(20):8224–8232, October 2022.

[29] Arghya Dutta, Emiko Mizuki, Yuka Tomori, and Shoichi Matsuda. Optimizing discharge rate for Li metal stability in rechargeable Li|NMC batteries under lean electrolyte condition. *ACS Appl. Energy Mater.*, 7(9):3824–3830, May 2024.

[30] Xia Cao, Hao Jia, Wu Xu, and Ji-Guang Zhang. Review—localized high-concentration electrolytes for lithium batteries. *J. Electrochem. Soc.*, 168(1):10522, January 2021.

[31] Denis Y. W. Yu, Kazunori Donoue, Takao Inoue, Masahisa Fujimoto, and Shin Fujitani. Effect of electrode parameters on $LiFePO_4$ cathodes. *J. Electrochem. Soc.*, 153(5):A835, 2006.

[32] Honghe Zheng, Jing Li, Xiangyun Song, Gao Liu, and Vincent S. Battaglia. A comprehensive understanding of electrode thickness effects on the electrochemical performances of Li-ion battery cathodes. *Electrochim. Acta*, 71:258–265, June 2012.

[33] Lee Loong Wong, Haomin Chen, and Stefan Adams. Design of fast ion conducting cathode materials for grid-scale sodium-ion batteries. *Phys. Chem. Chem. Phys.*, 19(11):7506–7523, 2017.

[34] C. Heubner, J. Seeba, T. Liebmann, A. Nickol, S. Bö rner, M. Fritsch, K. Nikolowski, M. Wolter, M. Schneider, and A. Michaelis. Semi-empirical master curve concept describing the rate capability of lithium insertion electrodes. *J. Power Sources*, 380:83–91, March 2018.

[35] Ruiyuan Tian, Sang-Hoon Park, Paul J. King, Graeme Cunningham, João Coelho, Valeria Nicolosi, and Jonathan N. Coleman. Quantifying the factors limiting rate performance in battery electrodes. *Nat. Commun.*, 10(1):1933, April 2019.

[36] Sang-Hoon Park, Ruiyuan Tian, João Coelho, Valeria Nicolosi, and Jonathan N. Coleman. Quantifying the trade-off between absolute capacity and rate performance in battery electrodes. *Adv. Energy Mater.*, 9(33):1901359, September 2019.

[37] Zhengyu Ju, Yue Zhu, Xiao Zhang, Diana M. Lutz, Zhiwei Fang, Kenneth J. Takeuchi, Esther S. Takeuchi, Amy C. Marschilok, and Guihua Yu. Understanding thickness-dependent transport kinetics in nanosheet-based battery electrodes. *Chem. Mater.*, 32(4):1684–1692, February 2020.

[38] Christian Heubner, Michael Schneider, and Alexander Michaelis. Diffusion-limited C-rate: A fundamental principle quantifying the intrinsic limits of Li-ion batteries. *Adv. Energy Mater.*, 10(2):1902523, January 2020.

[39] Ruiyuan Tian, Paul J. King, João Coelho, Sang-Hoon Park, Dominik V. Horvath, Valeria Nicolosi, Colm O'Dwyer, and Jonathan N. Coleman. Using chronoamperometry to rapidly measure and quantitatively analyse rate-performance in battery electrodes. *J. Power Sources*, 468:228220, August 2020.

[40] Dominik V. Horváth, João Coelho, Ruiyuan Tian, Valeria Nicolosi, and Jonathan N. Coleman. Quantifying the dependence of battery rate performance on electrode thickness. *ACS Appl. Energy Mater.*, 3(10):10154–10163, October 2020.

[41] Raymond B. Smith and Martin Z. Bazant. Multiphase porous electrode theory. *J. Electrochem. Soc.*, 164(11):E3291–E3310, 2017.

[42] Chixia Tian, Feng Lin, and Marca M. Doeff. Electrochemical characteristics of layered transition metal oxide cathode materials for lithium ion batteries: Surface, bulk behavior, and thermal properties. *Acc. Chem. Res.*, 51(1):89–96, January 2018.

[43] Jianyuan Li, Cong Lin, Mouyi Weng, Yi Qiu, Pohua Chen, Kai Yang, Weiyuan Huang, Yuexian Hong, Jian Li, Mingjian Zhang, Cheng Dong, Wenguang Zhao, Zhi Xu, Xi Wang, Kang Xu, Junliang Sun, and Feng Pan. Structural origin of the high-voltage instability of lithium cobalt oxide. *Nat. Nanotechnol.*, 16(5):599–605, May 2021.

[44] Xiaoyu Zhang, Martijn Van Hulzen, Deepak P. Singh, Alex Brownrigg, Jonathan P. Wright, Niels H. Van Dijk, and Marnix Wagemaker. Direct view on the phase evolution

in individual LiFePO4 nanoparticles during Li-ion battery cycling. *Nat. Commun.*, 6(1):8333, September 2015.

[45] Mikhael D. Levi, Sergey Sigalov, Gregory Salitra, Prasant Nayak, Doron Aurbach, Leonid Daikhin, Emilie Perre, and Volker Presser. Collective phase transition dynamics in microarray composite Li $_x$FePO$_4$ electrodes tracked by in situ electrochemical quartz crystal admittance. *J. Phys. Chem. C*, 117(30):15505–15514, August 2013.

[46] Atsuo Yamada, Hiroshi Koizumi, Shin-ichi Nishimura, Noriyuki Sonoyama, Ryoji Kanno, Masao Yonemura, Tatsuya Nakamura, and Yo Kobayashi. Room-temperature miscibility gap in LixFePO4. *Nature Mater*, 5(5):357–360, May 2006.

[47] Peng Bai, Daniel A. Cogswell, and Martin Z. Bazant. Suppression of phase separation in LiFePO$_4$ nanoparticles during battery discharge. *Nano Lett.*, 11(11):4890–4896, November 2011.

[48] Peng Bai and Guangyu Tian. Statistical kinetics of phase-transforming nanoparticles in LiFePO4 porous electrodes. *Electrochim. Acta*, 89:644–651, February 2013.

[49] Gosuke Oyama, Yuki Yamada, Ryu-ichi Natsui, Shin-ichi Nishimura, and Atsuo Yamada. Kinetics of nucleation and growth in two-phase electrochemical reaction of Li$_x$FePO $_4$. *J. Phys. Chem. C*, 116(13):7306–7311, April 2012.

[50] John S. Newman and Charles W. Tobias. Theoretical analysis of current distribution in porous electrodes. *J. Electrochem. Soc.*, 109(12):1183, 1962.

[51] Thomas M. Higgins and Jonathan N. Coleman. Avoiding resistance limitations in high-performance transparent supercapacitor electrodes based on large-area, high-conductivity PEDOT:PSS films. *ACS Appl. Mater. Interfaces*, 7(30):16495–16506, August 2015.

[52] Chih-Hsuan Hung, Phong Huynh, Katrina Teo, and Corie L. Cobb. Are three-dimensional batteries beneficial? Analyzing historical data to elucidate performance advantages. *ACS Energy Lett.*, 8(1):296–305, January 2023.

[53] John Newman. Optimization of porosity and thickness of a battery electrode by means of a reaction-zone model. *J. Electrochem. Soc.*, 142(1):97–101, January 1995.

[54] B.V. Ratnakumar, M.C. Smart, L.D. Whitcanack, and R.C. Ewell. The impedance characteristics of Mars exploration rover Li-ion batteries. *J. Power Sources*, 159(2):1428–1439, September 2006.

[55] C. Heubner, S. Reuber, J. Seeba, P. Marcinkowski, K. Nikolowski, M. Schneider, M. Wolter, and A. Michaelis. Application-oriented modeling and optimization of tailored Li-ion batteries using the concept of diffusion limited C-rate. *J. Power Sources*, 479:228704, December 2020.

[56] Alireza Soleimany Mehranjani, Mohammad Golmohammad, Shahriar Bozorgmehri, and Hamid Abdoli. A timescale characterization of (NMC811)/SiOx-graphite 1Ah pouch cell: Improving cycling stability with carbonate-based electrolytes and triallyl phosphate (TAP) co-additive. *J. Power Sources*, 602:234356, May 2024.

[57] Yiyang Li, Farid El Gabaly, Todd R. Ferguson, Raymond B. Smith, Norman C. Bartelt, Joshua D. Sugar, Kyle R. Fenton, Daniel A. Cogswell, A. L. David Kilcoyne, Tolek Tyliszczak, Martin Z. Bazant, and William C. Chueh. Current-induced transition from particle-by-particle to concurrent intercalation in phase-separating battery electrodes. *Nat. Mater.*, 13(12):1149–1156, December 2014.

[58] Shichun Yang, Chaochao Zhou, Qiong Wang, Binbin Chen, Yan Zhao, Bin Guo, Zhengjie Zhang, Xinlei Gao, Ridwanur Chowdhury, Huizhi Wang, Chao Lai, Nigel P. Brandon, Billy Wu, and Xinhua Liu. Highly aligned ultra-thick gel-based cathodes unlocking ultra-high energy density batteries. *Energy Environ. Mater.*, 5(4):1332–1339, October 2022.

[59] Zhonggang Liu, Junlu Zhu, Dongzhen Lu, Wei Wang, Liguo Yue, and Yunyong Li. Fabricating ultrathick, dense electrodes for compact rechargeable batteries with ultrahigh areal and volumetric capacity. *J. Power Sources*, 523:231046, March 2022.

[60] Shuhong Jiao, Jianming Zheng, Qiuyan Li, Xing Li, Mark H. Engelhard, Ruiguo Cao, Ji-Guang Zhang, and Wu Xu. Behavior of lithium metal anodes under various capacity utilization and high current density in lithium metal batteries. *Joule*, 2(1):110–124, January 2018.

[61] Elena Markevich, Gregory Salitra, Frederick Chesneau, Michael Schmidt, and Doron Aurbach. Very stable lithium metal stripping–plating at a high rate and high areal capacity in fluoroethylene carbonate-based organic electrolyte solution. *ACS Energy Lett.*, 2(6):1321–1326, June 2017.

[62] Zhaohui Wu, Haodong Liu, John Holoubek, Cassidy Anderson, Lili Shi, Hridayanand Khemchandani, Dongping Lu, Dianying Liu, Chaojiang Niu, Jie Xiao, and Ping Liu. The role of ion transport in the failure of high areal capacity Li metal batteries. *ACS Energy Lett.*, 7(8):2701–2710, August 2022.

[63] Oumaima Chaouachi, Jean-Michel Réty, Sylvie Génies, Marion Chandesris, and Yann Bultel. Experimental and theoretical investigation of Li-ion battery active materials properties: Application to a graphite/Ni0.6Mn0 .2Co0.2O2 system. *Electrochim. Acta*, 366:137428, January 2021.

[64] Ying Zhao, Peter Stein, Yang Bai, Mamun Al-Siraj, Yangyiwei Yang, and Bai-Xiang Xu. A review on modeling of electro-chemo-mechanics in lithium-ion batteries. *J. Power Sources*, 413:259–283, February 2019.

[65] Xuanchen Zhu, Ying Chen, Haofeng Chen, and Weiling Luan. The diffusion induced stress and cracking behaviour of primary particle for Li-ion battery electrode. *Int. J. Mech. Sci.*, 178:105608, July 2020.

[66] Lars Ole Valoen and Jan N. Reimers. Transport properties of $LiPF_6$-based Li-ion battery electrolytes. *J. Electrochem. Soc.*, 152(5):A882, 2005.

[67] John Newman and Nitash P. Balsara. *Electrochemical Systems*. The Electrochemical Society, fourth edition edition, 2021.